

The GSI capability to assimilate TRMM and GPM hydrometeor retrievals in HWRF

Ting-Chi Wu,^{a*} Milija Zupanski,^a Lewis D. Grasso,^a Paula J. Brown,^b Christian D. Kummerow^{a,b} and John A. Knaff^c

^aCooperative Institute for Research in the Atmosphere, Colorado State University, Fort Collins, CO, USA

^bDepartment of Atmospheric Science, Colorado State University, Fort Collins, CO, USA

^cNOAA/Center for Satellite Applications and Research, Fort Collins, CO, USA

*Correspondence to: T.-C. Wu, Cooperative Institute for Research in the Atmosphere, Colorado State University, 1375 Campus Delivery, Fort Collins, CO 80523-1375, USA. E-mail: ting-chi.wu@colostate.edu

This article has been contributed to by US Government employees and their work is in the public domain in the USA.

Hurricane forecasting skills may be improved by utilizing increased precipitation observations available from the Global Precipitation Measurement mission (GPM). This study adds to the Gridpoint Statistical Interpolation (GSI) capability to assimilate satellite-retrieved hydrometeor profile data in the operational Hurricane Weather Research and Forecasting (HWRF) system. The newly developed Hurricane Goddard Profiling (GPROF) algorithm produces Tropical Rainfall Measuring Mission (TRMM)/GPM hydrometeor retrievals specifically for hurricanes. Two new observation operators are developed and implemented in GSI to assimilate Hurricane GPROF retrieved hydrometeors in HWRF. They are based on the assumption that all water vapour in excess of saturation with respect to ice or liquid is immediately condensed out. Two sets of single observation experiments that include assimilation of solid or liquid hydrometeor from Hurricane GPROF are performed. Results suggest that assimilating single retrieved solid or liquid hydrometeor information impacts the current set of control variables of GSI by adjusting the environment that includes temperature, pressure and moisture fields toward saturation with respect to ice or liquid. These results are explained in a physically consistent manner, implying satisfactory observation operators and meaningful structure of background error covariance employed by GSI. Applied to two real hurricane cases, *Leslie* (2012) and *Gonzalo* (2014), the assimilation of the Hurricane GPROF data in the innermost domain of HWRF shows a physically reasonable adjustment and an improvement of the analysis compared to observations. However, the impact of assimilating the Hurricane GPROF retrieved hydrometeors on the subsequent HWRF forecasts, measured by hurricane tracks, intensities, sizes, satellite-retrieved rain rates, and corresponding infrared images, is inconclusive. Possible causes are discussed.

Key Words: satellite data assimilation; TRMM; GPM; hurricane forecasting; HWRF

Received 19 November 2015; Revised 2 June 2016; Accepted 22 June 2016; Published online in Wiley Online Library 30 August 2016

1. Introduction

One of the most urgent goals in the National Oceanic and Atmospheric Administration (NOAA), National Centers for Environmental Prediction (NCEP), and many other international numerical weather prediction (NWP) centres is to improve hurricane forecasts (e.g. NOAA, 2010). In addition to hurricane track and intensity predictions, precipitation forecasts have received significant attention due to the high-impact flooding and/or landslides from heavy rains worldwide (e.g. Yu *et al.*, 2014). With more satellite precipitation observations available through the Global Precipitation Measurement mission (GPM) constellation, NWP hurricane forecasting skills may be improved

via data assimilation. A combination of existing regional hurricane models and advanced data assimilation techniques are well suited to take advantage of the additional satellite precipitation observations. One available tool is the Hurricane Weather Research and Forecasting model (HWRF) that utilizes not only an advanced data assimilation component, but also a forecasting component (Tallapragada *et al.*, 2014).

HWRF is a coupled atmosphere–ocean dynamic forecast model that is run operationally by NCEP to support the National Hurricane Center (NHC) on the tropical cyclone track and intensity forecast guidance (Rappaport *et al.*, 2009). Since the initial implementation of HWRF in 2007, many systematic developments and upgrades have occurred within HWRF throughout the

years (Bernardet *et al.*, 2015). The latest release of the operational system (HWRF version 3.7a: Tallapragada *et al.*, 2015) is configured with triply nested domains: the parent domain and two moving nested domains with 18, 6 and 2 km horizontal grid spacing, respectively. A vortex initialization procedure and a data assimilation system based on the Gridpoint Statistical Interpolation (GSI: Wu *et al.*, 2002) are employed to optimize the storm-scale initial conditions for an HWRF forecast. Conventional observations and satellite observations restricted to clear-sky regions are assimilated into the intermediate domain. Satellite radiances are generally not assimilated in the innermost domain.

Both Tropical Rainfall Measuring Mission (TRMM: Simpson *et al.*, 1996) and its successor, the Global Precipitation Measurement missions (GPM: Hou *et al.*, 2014), provide remote observations of the Earth–atmosphere system. In addition, they also provide a relatively wide swath of data that is used to retrieve precipitation rates and information about the vertical structure of hydrometeors from the Goddard Profiling (GPROF) algorithm (Kummerow *et al.*, 2001, 2015). Remote observations of precipitation characteristics can provide useful information about tropical cyclone development; in particular, precipitation structures like spiral bands and an eyewall that are concealed by a central dense overcast (Hence and Houze, 2012), and differentiating areas of non-precipitating, stratiform precipitation, and convective precipitation. Assimilation of TRMM-retrieved rain rates has been found to improve the forecast of tropical cyclone structure and precipitation (Pu *et al.*, 2002; Hou *et al.*, 2004; Kumar *et al.*, 2014). Because GPM is relatively new (launched in 2014), there are few studies that have utilized GPM precipitation data for hurricane forecasts. Of the few studies, data assimilation techniques and strategies to assimilate GPM radiances affected by precipitation have been developed (Zupanski *et al.*, 2011; Zhang *et al.*, 2013b; Chambon *et al.*, 2014).

This study extends previous work by using the operational configuration of HWRF to include the capability to assimilate satellite-retrieved precipitation data and to examine the impact in the innermost domain of HWRF. There is a conceptual distinction between the assimilation of satellite *radiances* and the assimilation of *retrieved quantities* from satellite radiances. Satellite radiances are not assimilated in the innermost domain of HWRF; however, in this study, a retrieved quantity like hydrometeor profiles is assimilated in the innermost domain of HWRF.

To facilitate this effort, a newly developed variation of the GPROF algorithm called Hurricane GPROF (Brown *et al.*, 2016) is used in this study. It utilizes observations from TRMM and GPM sensors to provide retrieved rain rates and hydrometeor profiles specifically for hurricanes. Those retrieved hydrometeor quantities are assimilated into HWRF. Since hydrometeor profiles from Hurricane GPROF are introduced into HWRF for the first time, new observation operators are developed and implemented into the GSI data assimilation system within HWRF. Using these new capabilities, this study explores the impacts of assimilating satellite-retrieved hydrometeor quantities in the innermost domain of HWRF.

This article concentrates on results obtained from experiments with two Atlantic hurricanes, Hurricane *Leslie* (2012), and Hurricane *Gonzalo* (2014), and is organized as follows. An overview of the retrieved hydrometeors from TRMM and GPM, and the methodology of assimilating the Hurricane GPROF hydrometeor retrievals in HWRF are discussed in sections 2 and 3. Results from the experiments are presented in section 4, while section 5 details information related to the resulting HWRF forecasts. Finally, a summary and discussion along with some thoughts on future work are contained in section 6.

2. Satellite-retrieved hydrometeors

2.1. TRMM and GPM data

TRMM was launched in November 1997 to provide remote sensing of moderate to heavy rain events. Two principal

precipitation measurement instruments on TRMM are the TRMM Microwave Imager (TMI) and the precipitation radar (PR). Precipitation retrievals are based on the emission of microwave radiation from raindrops that appears warm against a cooler ocean background. After 17 years of service, the TRMM mission came to an end in 2014. In February 2014, GPM was launched to continue, expand and improve the observations of global precipitation. There are two instruments that make up the GPM Core Observatory. One is the GPM Microwave Imager (GMI) and the other is the Dual-frequency Precipitation Radar (DPR). By including four channels whose frequencies are greater than 166 GHz, GMI is capable of retrieving a wide spectrum of precipitation intensities. Additional details of both TRMM and GPM are described in Kummerow *et al.* (1998) and Hou *et al.* (2014), respectively. Data from both platforms are used in hydrometeor retrievals.

2.2. Hydrometeor retrieval

Several types of hydrometeor retrieval algorithms exist that could be used with TRMM and GPM observations. One type of algorithm that uses data from the corresponding precipitation radars on TRMM and GPM (PR and DPR, respectively) retrieves rain rates and vertical profiles of hydrometeors (e.g. Iguchi *et al.*, 2000). However, a characteristic of the data from PR and DPR is that the swath width is generally smaller than a tropical cyclone. A second type of algorithm uses data from the corresponding imagers on TRMM and GPM (TMI and GMI, respectively) to retrieve rain rates and vertical profiles of hydrometeors. Unlike the relatively narrow swath width of both PR and DPR, the swath width of data from both TMI and GMI is large enough to observe the whole tropical cyclone. The second type of algorithm is referred to as the Goddard PROFiling algorithm (GPROF: Kummerow *et al.*, 2001), which at present is called GPROF 2014 (Kummerow *et al.*, 2015). In addition, there is a customized retrieval algorithm for hurricane applications, referred to as Hurricane GPROF (Brown *et al.*, 2016). Hurricane GPROF improves the GPROF 2014 retrievals in hurricane scenes by using a combination of (i) an empirical database that is developed from both PR and TMI, (ii) best-track information contained in HURricane DATa 2nd generation (HURDAT2: Landsea and Franklin, 2013), and (iii) GPROF 2014 retrievals. Retrieved vertical profiles of hydrometeors from Hurricane GPROF are used in this study.

2.3. Preparation of Hurricane GPROF retrievals for assimilation

Hurricane GPROF retrievals include vertical profiles of four hydrometeor types: (i) ice, (ii) mixed-phase, (iii) rain, and (iv) cloud water (kg m^{-3}). In order to adjust for the capabilities of the HWRF modelling and data assimilation system, a decision is made to assimilate integrated values of vertical profiles of hydrometeors. This decision will likely produce better results because observation errors of vertical profiles are anticipated to be larger than the errors of the corresponding vertically integrated values. Assuming that errors of vertical profile are random and unbiased, as is normally done in data assimilation, it is likely that the sum of errors of a vertical profile will have cancellations due to errors with opposite signs, making the errors of integrated values smaller. In actuality, there are several possible sources of additional errors that are associated with vertical profiles. The operational HWRF model has total cloud condensate (referred to as CWM) as prognostic variable instead of individual hydrometeor types. If one would like to assimilate vertical profiles of hydrometeors with GSI, a procedure that converts CWM into individual hydrometeors types would have to be used, thus introducing additional errors. Another possible source of observation errors is the use of prescribed profiles in the Hurricane GPROF algorithm (Brown *et al.*, 2016). All these factors suggest that assimilation of

integrated values of hydrometeor profiles can be advantageous in this system.

Prior to vertical integration, four vertical profiles are transformed into two vertical profiles to simplify the data assimilation procedure. The two vertical profiles are solid condensate, referred to as solid-water content (SWC), and liquid condensate, referred to as liquid-water content (LWC). The SWC profile was made by adding values of the upper half of the mixed-phase profile to the corresponding values of the ice profile; the LWC profile was made by adding values of the lower half of the mixed-phase profile to the corresponding values of the cloud and rain profiles. Finally, vertical integration was performed to yield an integrated value, one for SWC and one for LWC. Each of these values is then assimilated along with new observation operators.

3. Methodology for assimilating retrieved integrated SWC and LWC in HWRF

3.1. NOAA operational HWRF (2014 implementation)

The HWRF version 3.6a (Tallapragada *et al.*, 2014), which is functionally equivalent to the 2014 operational version of HWRF, is employed in this study. Modelling components in HWRF include (i) the Weather Research and Forecast model (WRF) software infrastructure, (ii) the Nonhydrostatic Mesoscale Model (NMM: Janjic, 2003) dynamic core, (iii) the Princeton Ocean Model for Tropical Cyclones (POM-TC: Yablonsky *et al.*, 2015), and (iv) the NCEP coupler which acts as an independent interface between the atmosphere and ocean components. The initialization portion of HWRF uses a vortex initialization package and the HWRF Data Assimilation System, which is a GSI-based regional hybrid variational-ensemble data assimilation system.

There exist many options in the configuration of the operational HWRF. Some of the main options in the configurations are the Geophysical Fluid Dynamics Laboratory (GFDL) surface layer scheme, the GFDL slab land-surface model, a modified GFDL long-wave and short-wave scheme, the modified Ferrier microphysics scheme for the Tropics (Ferrier, 2005), the simplified Arakawa-Schubert (SAS) cumulus scheme, and the NCEP Global Forecasting System (GFS) boundary-layer parametrization. Additional details of physics options in HWRF can be found in Tallapragada *et al.* (2014).

In HWRF version 3.6a, the NMM core is configured with three domains and they are referred to as d01, d02 and d03. Those domains use a horizontal grid spacing of 27, 9 and 3 km, respectively. The size of domain 1 is about 5900 km × 5900 km; similarly, the size of domain 2 is about 960 km × 960 km, and the size of domain 3 is about 600 km × 600 km (Figure 1). Domain 3 is nested in domain 2, and domain 2 is nested in domain 1; furthermore, both d02 and d03 are storm-relative moving grids. Both inner nests are two-way interactive grids. To allow more observations to be assimilated in a hurricane and its near environments, both d02 and d03 are extended to a larger size and they are referred to as ghost d02 (about 1500 km × 1500 km) and ghost d03 (about 750 km × 750 km) (Figure 1). After GSI data assimilation, ghost d02 and ghost d03 are then interpolated back to the d02 and d03 domains as initial conditions for HWRF forecasts. There are 61 vertical levels and the model top extends to 2 hPa. The POM-TC is configured with a single trans-Atlantic ocean domain for the North Atlantic basin and three-dimensional coupling for the east Pacific basin.

3.2. GSI and vortex initialization

HWRF data assimilation component utilizes GSI with a regional one-way hybrid ensemble-3D-Var data assimilation scheme (Wang, 2010). Background error covariance of the hybrid system is a combination of the static background error covariance embedded in GSI (Parrish and Derber, 1992; Wu *et al.*, 2002; Kleist *et al.*, 2009) and the flow-dependent background error covariance

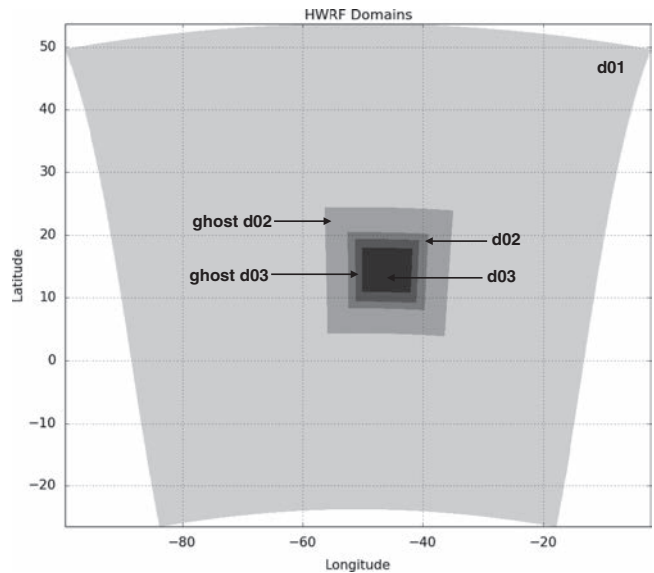


Figure 1. HWRF model forecast domains, as indicated by d01, d02, and d03, and HWRF data assimilation domains, as indicated by ghost d02 and ghost d03.

estimated from the NCEP operational GFS 80-member ensemble forecast (T254L64) at a resolution of approximately 55 km. The static background error covariance is determined using the recursive filter (Purser *et al.*, 2003) on the analysis grid, which is $\sqrt{2}\Delta x$ where Δx is the grid spacing of HWRF domains. In a 3D-Var system, observations at different times are compared to only one background (also known as first guess) field. One optional aspect of GSI is to include additional background fields through the use of the First Guess at Appropriate Time (FGAT). FGAT is employed in GSI to assimilate observations over a time window by interpolating a time sequence of background fields to the actual observation times (Lorenz and Rawlins, 2005). Currently, three background files that are valid at -3 , 0 and $+3$ h from the actual analysis time within a 6 h time interval are used. Control variables in the operational GSI include stream function, velocity potential, temperature, specific humidity, surface pressure and ozone.

As part of the generation of a background field, the Global Data Assimilation System (GDAS) forecast is used. In addition to GDAS, either the storm vortex from a previous HWRF forecast or a bogus vortex will be used, depending upon the observed vortex intensity and the availability of a previous cycle that includes an HWRF forecast and an analysis. In the vortex initialization procedure, relocation, resizing, and intensity-correction were performed on the vortex based on the Tropical Cyclone Vitals Database (TCVitals*). More details of the vortex initialization process can be found in Tallapragada *et al.* (2014).

After vortex initialization, observations are assimilated by GSI. Observational data assimilated in GSI are categorized into conventional† and satellite data. Satellite data assimilated in GSI includes both retrievals (including satellite-derived winds and the GPS Radio Occultation data) and radiances. Satellite radiances can be categorized into clear sky or cloudy sky. Currently, GSI assimilates clear-sky radiances from several geostationary

*TCVitals is an archive of Cyclone Message Files, which contain cyclone location, intensity, and structure information, created in real time by forecasting centres. Available online at http://www.emc.ncep.noaa.gov/mmb/data_processing/tcvitals_description.htm. These data are used to initialize tropical cyclone forecasts in several NCEP operational models via vortex bogus and vortex relocation methods.

†Conventional observations assimilated in operational GSI include radiosondes, dropwindsondes, aircraft reports, surface ship and buoy observations, surface observations overland, pibal winds, wind profilers, radar-derived Velocity Azimuth Display (VAD) wind, WindSat scatterometer winds, integrated precipitable water derived from the Global Positioning System (GPS). The NOAA P3 Tail Doppler Radar (TDR) radial winds are also assimilated in ghost d03 when they are available.

and polar-orbiting satellites. In an operational setting, GSI data assimilation is performed within both ghost d02 and ghost d03. Conventional and satellite data are assimilated within ghost d02 while only conventional data are assimilated within ghost d03. This study extends the operational configuration by including satellite data assimilation within ghost d03 and exploring the usage of TRMM- and GPM-retrieved integrated SWC and LWC.

3.3. Observation operators for integrated SWC and LWC

In order to assimilate TRMM- and GPM-retrieved integrated SWC and integrated LWC, new observation operators (also known as a forward operator) along with the corresponding tangent linear and adjoint components are developed for this study. One possible choice of implementing the observation operators in this study would be to add hydrometeor mass mixing ratios to the current set of control variables. However, the resulting changes in initial conditions of hydrometeors would have to be dynamically consistent with changes in the environment in initial conditions (such as temperature T , specific humidity q , and surface pressure ps), in order to support the existence of clouds/hydrometeors in the subsequent forecast. Such changes in the environment rely on cross-variable correlations between hydrometeor mass mixing ratios and the environment, defined by the background error covariance in the operational (i.e. hybrid) GSI. Unfortunately, the above-mentioned cross-variable correlations do not exist in the static background error covariance. On the other hand, the ensemble component of the background error covariance is obtained from the operational GFS 80-member ensemble forecasts (a model different from HWRF) that have relatively coarse resolution. In addition, the hydrometeor mass mixing ratios are set to zero during the vortex initialization procedure, implying that the background field is in clear-sky condition. Although this could be avoided, it would require changes in the operational HWRF procedures (including vortex initialization and data assimilation). Due to the above-mentioned limitations, we choose to implement observation operators in such a way that the initial conditions that include T , q and ps (used to infer three-dimensional pressure, P) are adjusted to support the existence of hydrometeors. The observations operators will be built under the operational configuration to extend the impact of assimilating integrated SWC and LWC to the current set of GSI control variables.

As part of the development of the new observation operators, the main assumption is that all water vapour in excess of saturation is immediately condensed out (Cotton, 1972; Thompson *et al.*, 2004; Morrison *et al.*, 2005). The SWC and LWC of the retrievals are then approximated by the excess of saturation with respect to either ice or liquid water. The observation operator is then defined as a vertical integration of water vapour mixing ratio (kg kg^{-1}) in excess of saturation with respect to ice or liquid. However, such a defined observation operator is likely to underestimate the integrated water contents and thus lead to a negative bias of the background guess compared to the observed value. We will address this issue later.

Thus, the observation operator for integrated SWC, h_s , is

$$h_s = \begin{cases} \sum_{k=k_0}^{k_{\max}} (q_v^k - q_{si}^k) \rho^k \Delta z^k & \text{if } q_v^k \geq q_{si}^k \\ 0 & \text{if } q_v^k < q_{si}^k \end{cases}, \quad (1)$$

where q_v is water vapour mixing ratio, q_{si} is saturation mixing ratio with respect to ice, ρ is air mass density and can be inferred using T , P and q_v , and Δz is layer thickness. The superscript k denotes the model vertical level index, k_0 is the vertical level where temperature is $T_0 = 273.16$ K, and k_{\max} is the index for the top model level. Similarly, the observation operator for integrated

Table 1. Constants used by the Clausius–Clapeyron equation.

C_1	C_2
$C_1^{\text{ice}} = -(S_{\text{vapour}} - S_{\text{solid}})/R_v$	$C_2^{\text{ice}} = C_1^{\text{ice}} + (L_{\text{vapor}} + L_{\text{fusion}})/R_v T_0$
$C_1^{\text{liquid}} = -(S_{\text{vapour}} - S_{\text{liquid}})/R_v$	$C_2^{\text{liquid}} = C_1^{\text{liquid}} + (L_{\text{vapor}}/R_v T_0)$
S_{vapour} : specific heat of water vapour = $1.846 \times 10^3 \text{ J kg}^{-1} \text{ K}^{-1}$	
S_{liquid} : specific heat of liquid water = $4.190 \times 10^3 \text{ J kg}^{-1} \text{ K}^{-1}$	
S_{solid} : specific heat of ice water = $2.106 \times 10^3 \text{ J kg}^{-1} \text{ K}^{-1}$	
R_v : gas constant of water vapour = $461.6 \text{ J kg}^{-1} \text{ K}^{-1}$	
L_{vapor} : latent heat of condensation = $2.5 \times 10^6 \text{ J kg}^{-1}$	
L_{fusion} : latent heat of fusion = $3.3358 \times 10^5 \text{ J kg}^{-1}$	

LWC, h_l , is

$$h_l = \begin{cases} \sum_{k=1}^{k_{\text{mix}}} (q_v^k - q_{sl}^k) \rho^k \Delta z^k & \text{if } q_v^k \geq q_{sl}^k \\ 0 & \text{if } q_v^k < q_{sl}^k \end{cases} \quad (2)$$

where q_{sl} is saturation mixing ratio with respect to liquid, and k_{mix} is the vertical level where temperature is $T_{\text{mix}} = 253.16$ K.

Since specific humidity (q) is one of the control variables that will be updated in GSI, a conversion from specific humidity to water vapour mixing ratio, $q_v = \frac{q}{1-q}$, is required. In addition, the computation of saturation mixing ratio with respect to both ice and liquid will be required. This is done through the use of the following two equations:

$$q_{si} = 0.622 \frac{e_{si}}{P - e_{si}} \quad (3)$$

and

$$q_{sl} = 0.622 \frac{e_{sl}}{P - e_{sl}} \quad (4)$$

where e_{si} and e_{sl} are the saturation vapour pressures with respect to ice and liquid. In Eqs (3) and (4), e_{si} and e_{sl} are only a function of temperature as described by the Clausius–Clapeyron equation[‡]:

$$e_s(T) = P_0 \left(\frac{T_0}{T} \right)^{C_1} \exp \left\{ C_2 \left(1 - \frac{T_0}{T} \right) \right\}, \quad (5)$$

where $T_0 = 273.16$ K, $P_0 = 610.78$ hPa, and there are two constants, C_1 and C_2 . Both C_1 and C_2 are non-dimensional constants and have ice and liquid components, C_1^{ice} , C_1^{liquid} , C_2^{ice} and C_2^{liquid} (Table 1). As a result, the saturation vapour pressure with respect to ice and liquid can be expressed by

$$e_{si}(T) = P_0 \left(\frac{T_0}{T} \right)^{C_1^{\text{ice}}} \exp \left\{ C_2^{\text{ice}} \left(1 - \frac{T_0}{T} \right) \right\} \quad \text{for } T < T_{\text{mix}} \quad (6)$$

and

$$e_{sl}(T) = P_0 \left(\frac{T_0}{T} \right)^{C_1^{\text{liquid}}} \exp \left\{ C_2^{\text{liquid}} \left(1 - \frac{T_0}{T} \right) \right\} \quad \text{for } T > T_0. \quad (7)$$

In Eqs (1) and (2), the observation operator for integrated SWC is applied for temperatures below T_0 and the observation operator for integrated LWC is applied for temperatures above T_{mix} . For temperatures within the interval (T_{mix}, T_0) where a

[‡]For additional information about the Clausius–Clapeyron equation, the interested readers can refer to section 4.4 in Emanuel (1994).

mixture of SWC and LWC may exist, saturation vapour pressure is computed by linearly combining Eqs (6) and (7):

$$e_s(T) = w \cdot e_{sl}(T) + (1 - w) \cdot e_{si}(T), \quad (8)$$

where the weighting coefficient $w = (T - T_0)/(T_0 - T_{\text{mix}})$. Equations (6)–(8) and w together are used in GSI to compute saturation vapour pressure for three specific temperature ranges; $T < T_{\text{mix}}$, $T > T_0$, and $T_{\text{mix}} < T < T_0$. This three-equation formulation defines a piecewise continuous function of temperature. Since temperature is one of the control variables in GSI, calculation of a temperature gradient during the cost function minimization process using the above-mentioned weight coefficient will likely introduce discontinuities at T_{mix} and T_0 . To avoid discontinuities, an alternate version of the weighting coefficient is implemented, following Zupanski (1993): $w = 0.5\{1 + \tanh(\Delta T)\}$, where $\Delta T = \{T - 0.5(T_{\text{mix}} + T_0)\}/\{0.25(T_0 - T_{\text{mix}})\}$. As a result, a single equation, Eq. (8), with this new weighting coefficient is used to compute saturation vapour pressure for any given temperature. Equations (3) and (4) then become

$$\begin{cases} q_{si} & = 0.622 \frac{e_s(T)}{P - e_s(T)} & \text{if } T < T_0 \\ q_{sl} & & \text{if } T > T_{\text{mix}} \end{cases}, \quad (9)$$

where e_s is computed by Eq. (8) and the new w . Equation (9) is then used in both observation operators h_s and h_l , Eqs (1) and (2), in which both operators can be expressed as functions of the three variables that include T , P and q .

In addition, the derivatives of the operator with respect to T , P and q (often referred to as Jacobians) are also calculated and saved, implying that the tangent linear operator is a linear combination of perturbations of T , P and q , in which Jacobians are the corresponding coefficients (see Appendix). This also reduces the complexity of the adjoint operator, in which the same linear combination coefficients are used to compute gradients of perturbation in T , P and q .

As described in Wang (2010), in hybrid GSI, covariance localization is conducted in the model space not in observation space as for most ensemble data assimilation systems. The localization is applied to control variables in model grid space with prescribed correlation lengths. Therefore, no assumption about the explicit position of the observation is required during the procedure of the covariance localization.

Due to the introduction of new observation types (integrated SWC and integrated LWC) and new observation operators, Eqs (1) and (2), into the operational HWRF GSI system, single observation (1-OBS) experiments are conducted. The 1-OBS experiments are conducted to examine the influence of assimilating retrieved integrated SWC and integrated LWC on some of the state variables in GSI within a hurricane environment.

3.4. 1-OBS experiments

Two sets of two 1-OBS experiments are performed with an HWRF simulation of Hurricane *Leslie* (2012).⁵ The first set of experiments include 1-OBSSOLID and 1-OBSLIQUID, where a single observation of integrated SWC and integrated LWC with value of 0.5 kg m^{-2} is placed at 21.8°N , 60.0°W , about 150 km east of the centre of *Leslie* at 1800 UTC 2 September. The background guessed value of integrated SWC and integrated LWC at this location is 0.001 and 0 kg m^{-2} , respectively. The observation error is 0.5 kg m^{-2} for both integrated SWC and LWC observations. In the first set of experiments, GSI is performed without the hybrid option (i.e. static background error covariance only). Thus, the analysis from the first set of experiments represents results from

a 3D-Var assimilation. Similarly, the second set of experiments also includes 1-OBSSOLID and 1-OBSLIQUID. However, GSI is performed with the hybrid option (i.e. GFS ensemble forecasts are utilized in the background error covariance). Analyses from the second sets of experiments represent outputs from an ensemble-3D-Var assimilation. Results from these 1-OBS experiments highlight the influence of the integrated SWC and integrated LWC on state variables through the use of the new observation operators and background error covariance (Parrish and Derber, 1992). Visualization of the results will be shown by using an analysis increment (analysis minus background) from the 1-OBS experiments.

To begin with, output from both the 1-OBSSOLID and the 1-OBSLIQUID experiments neglecting the hybrid option is described. The analysis increments from 1-OBSSOLID are presented in an east–west vertical cross-section along the latitude of the location of the single observation that is 21.8°N as shown in Figure 2(a), (b) and (d). Values of the analysis increment in T are negative with a local minimum of about -0.02 K near 60°W and 400 hPa; implying a reduction of the values of the temperature in the analysis. A local maximum of about 0.024 g kg^{-1} near 60°W and 500 hPa in the analysis increment of q is evident in Figure 2(b), suggesting an increase of the values of q in the analysis field. Figure 2(c), which shows the analysis increment of the ps , indicates an increase in the values of the analysis increment of ps ; consequently, values of ps in the 1-OBSSOLID analysis increase. Figure 2(d) shows the response of the analysis increment of the v -component of the wind field to the inclusion of the integrated SWC. Similarly, Figure 2(e), (f) and (h) present the analysis increments from 1-OBSLIQUID in the same east–west cross-section as Figure 2(a), (b) and (d). Values of the analysis increment in T are negative with a local minimum of about -0.016 K near 60°W and surface, implying a reduction of the values of the temperature in the analysis. A local maximum of about 0.09 g kg^{-1} near 60°W and surface in the analysis increment of q is evident in Figure 2(f), suggesting an increase of the values of q in the analysis. Figure 2(g) exhibits a decrease in the values of the analysis increment of ps ; consequently, values of ps in the 1-OBSLIQUID analysis decrease. Response of the analysis increment of the v -component wind field to the inclusion of the integrated LWC is illustrated in Figure 2(h).

A reasonable physical interpretation is possible for these no-hybrid experiment results. Note that the q increments are positive in both Figure 2(b) and (f) in response to increased observation innovation. Similarly, the T increments are negative in both Figure 2(a) and (e) in response to approaching saturation with respect to ice/liquid water. In sharp contrast, the ps increments are of opposite signs in Figure 2(c) and (g). At first, such a result may seem contradictory. Resolution of the apparent contradiction may be provided through the use of the integrated form of the hydrostatic equation that can be expressed as:

$$P(z_l) = P(z_u) \cdot \exp\left(\frac{g(z_u - z_l)}{R_d \bar{T}_v}\right), \quad (10)$$

where z_u and z_l are the upper and lower physical heights, g is the acceleration due to gravity, R_d is the dry gas constant, and \bar{T}_v is the averaged virtual temperature in a layer between z_u and z_l . That is, the simulated atmosphere in the no-hybrid experiments is assumed to be in hydrostatic balance. The key variable to focus on in Eq. (10) is the virtual temperature: $\bar{T}_v = T(1 + 0.6 \cdot q_v)$.

Note that \bar{T}_v is a function of not only T , but also q_v . Consider the negative values of the T analysis increments (Figure 2(a)); they imply a decrease in T . By itself, a T decrease will act to decrease \bar{T}_v . Although there is a positive analysis increment of q (Figure 2(b); equivalent to a positive increment in q_v because $q_v = \frac{q}{1-q}$), values of q in the analysis are too small to offset the influence of T on \bar{T}_v . Therefore, values of \bar{T}_v in the analysis decrease. Since \bar{T}_v exists in the denominator in Eq. (10), the argument of the exponent increases, leading to an increase in

⁵Additional details about Hurricane *Leslie* (2012) are provided in a subsequent section.

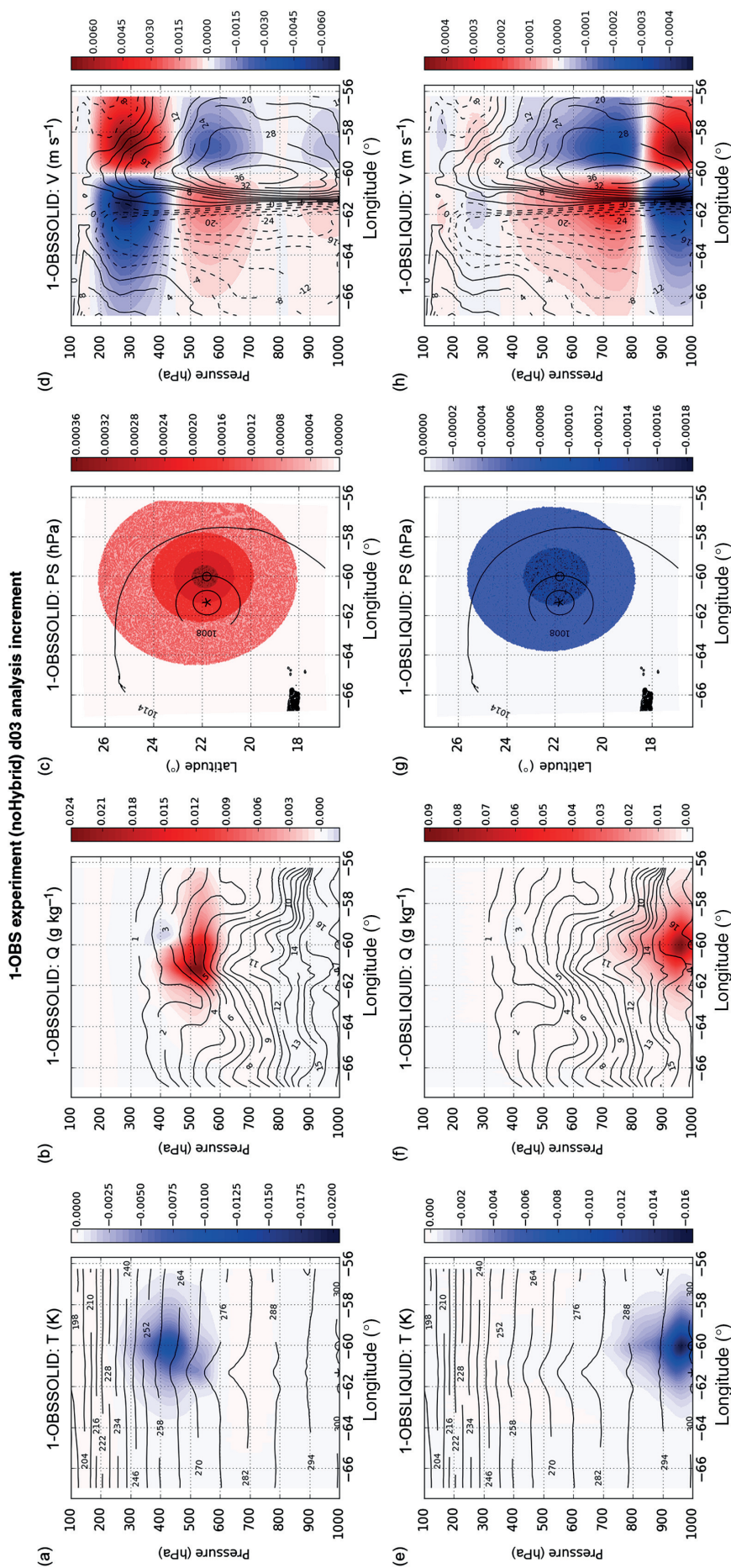


Figure 2. East-west cross-section of analysis increments (colour) overlapped with background field (contour) along the latitude (21.8°N) of the single observation location (open circle) from the no-hybrid 1-OBSLIQUID experiment: (a) temperature (K) and (b) specific humidity (g kg⁻¹), (c) Analysis increments in surface pressure (hPa), (d) Cross-section of analysis increments in v-component of wind fields (m s⁻¹), (e)–(h) Same as (a)–(d) except for analysis increments from the no-hybrid 1-OBSLIQUID experiment. Background field contains Hurricane Leslie (2012) at 1800 UTC 2 September.

ps (Figure 2(c)). In the lower troposphere, values of q can be approximately two orders of magnitude larger than those in the upper troposphere. As a result, relatively larger values of q in the lower troposphere can offset the influence of a T decrease on $\overline{T_v}$ (as inferred by Figure 2(e) and (f)), resulting in an increase in $\overline{T_v}$. An increase in $\overline{T_v}$ causes the argument of the exponent in Eq. (10) to increase, thus reducing ps (Figure 2(g)). The above analysis therefore provides a resolution to the apparent contradiction. In addition, wind adjustment (Figure 2(d) and (h)) can be understood via the mass–wind balance relationships prescribed in static background error covariance embedded in GSI (e.g. Parrish and Derber, 1992).

We now move on to results obtained when the hybrid option is used. In the hybrid experiments, the background error covariance comprises a linear weighting of 20% of the static 3D-Var error covariance that is embedded in GSI and 80% of the error covariance that originates within the GFS 80-member ensemble forecasts. This linear weighting follows the operational configuration of GSI. Thus, analysis increments from the hybrid experiments are expected to show a blended influence from both the static and flow-dependent background error covariance.

The region containing the dominant impacts in the hybrid experiments extends vertically through a significant portion of the simulated troposphere (Figure 3). In general, the response to the analysis increments of the above-mentioned fields in the hybrid experiments exhibits more spatial variability compared to the no-hybrid experiments. In addition, the magnitudes of the analysis increments are larger than the corresponding analysis increments from the no-hybrid experiments. While both no-hybrid and hybrid experiments assimilated the same observation and used the same observation operator, the only difference between the no-hybrid and hybrid experiments is through the use of a flow-dependent ensemble background error covariance. The difference is likely due to the cross-correlation (or cross-covariance) that is described differently between the static and ensemble background error covariance. Cross-correlation contains information about the relationship between different state variables. By giving a larger weight to the ensemble background error covariance (80%), the dominant responses to analysis increments are expected to mostly come from the ensemble component.

Interestingly, the dominant negative increments in T near 61°W and between 500 hPa and surface (Figure 3(a)) are approximately collocated with the positive increments in q (Figure 3(b)), suggesting lowering temperature and increasing moisture together to approach saturation. Similar collocated increments in T and q near 61°W and between 700 hPa and surface are evident in Figure 3(e) and (f). In addition, negative ps increments and dipoles of opposite signs of v increments (Figure 3(c), (d), (g) and (h)) show deepened surface pressure accompanied by enhanced low-level cyclonic flows in a physically consistent way. Although a concise physical interpretation is more challenging for the hybrid experiments, analysis increments of the four variables exhibit an adjustment from a background state to an analysis in a consistent way. These results, along with the no-hybrid experiments, suggest that the new observation operators are extending the impacts of assimilating new observations to the state variables in a physically consistent manner.

4. Data assimilation experiments

4.1. Case description

Both Hurricane *Leslie* (2012) and *Gonzalo* (2014) were long-lived and spent the majority of their lives in the Atlantic Ocean without making landfall at the continental USA. Their long lives allow sufficient TRMM and GPM observations to be collected. The detailed descriptions of these cases follow.

4.1.1. Hurricane *Leslie*

Leslie was a Category 1 hurricane that spanned the period from 30 August to 12 September 2012. *Leslie* developed from a tropical wave moving off the west coast of Africa, and strengthened into a tropical depression near the northern Leeward Islands around 30 August 2012. After acquiring tropical storm status, *Leslie* moved steadily west-northwestward and slowly intensified by 2 September. A high-latitude blocking pattern over Atlantic Canada resulted in weak steering currents that caused *Leslie* to drift slowly for 4 days. It was later upgraded to a Category 1 hurricane with maximum sustained wind speed of 65 kn at 0600 UTC on September 5 due to the weakened deep-layer shear (Stewart, 2013). A visible satellite image from the Geostationary Operational Environmental Satellite-13 (GOES-13) shows *Leslie* at its peak intensity, 70 kn at 1145 UTC 5 September 2012 (Figure 4(a)).

4.1.2. Hurricane *Gonzalo*

Gonzalo spanned the period of 12–20 October 2014. It was the strongest hurricane in the Atlantic since Hurricane *Igor* (2010). Unlike *Leslie*, *Gonzalo* became a tropical storm east of Antigua by 1200 UTC 12 October 2014 and quickly strengthened into a hurricane within 1 day. *Gonzalo* then turned west-northwestward and made landfall on Antigua, St Martin and Anguilla as a Category 1 hurricane at 1200 UTC on 13 October, causing damage to those and nearby islands. Shortly thereafter, *Gonzalo* moved northwestward as it rapidly intensified into a Category 4 major hurricane by 0000 UTC 15 October (Brown, 2015). The maximum sustained wind of 125 kn was observed at 1200 UTC 16 October when *Gonzalo* reached its peak intensity. Figure 4(b) shows *Gonzalo* in a visible image at 1145 UTC 16 October.

4.2. Experimental design

Two data-assimilation experiments are designed (Table 2) to evaluate the assimilation of Hurricane GPROF retrieved integrated SWC and LWC in the innermost domain of HWRF and they are as follows:

- (i) The control experiment (denoted by CTL) uses the 2014 HWRF operational configuration (i.e. hybrid option of GSI and other features mentioned in sections 3.1 and 3.2) that assimilates both conventional and satellite observations in ghost d02. In ghost d03, however, only conventional observations are assimilated.
- (ii) The second experiment (denoted by AddWC) is the same as (i). In addition to conventional observations, integrated SWC and LWC retrieved from Hurricane GPROF are also assimilated in ghost d03.

Both the CTL and the AddWC experiments are conducted for Hurricane *Leslie* (2012) and Hurricane *Gonzalo* (2014), respectively. Hurricane GPROF retrieved integrated SWC and LWC from TRMM are available near 0000 and 1800 UTC for *Leslie*. To assimilate the available retrievals in the 6 h cycling of GSI, HWRF is initialized on 1800 UTC and cycled through to 0000 UTC of the next day for Hurricane *Leslie* (2012).

Similarly, Hurricane GPROF retrieved integrated SWC and LWC from GPM for Hurricane *Gonzalo* (2014) are available near 0600 and 1200 UTC, and occasionally near 0000 UTC. To be consistent with the experimental design for *Leslie*, the first cycle for *Gonzalo* starts at 0600 UTC with the second cycle on 1200 UTC. If there are no Hurricane GPROF retrieved observations available on 1200 UTC, the first cycle will be starting at 0000 UTC with the second cycle on 0600 UTC.

Due to the data availability mentioned above, only two consecutive cycles that assimilate the Hurricane GPROF retrievals are conducted for both *Gonzalo* and *Leslie*.

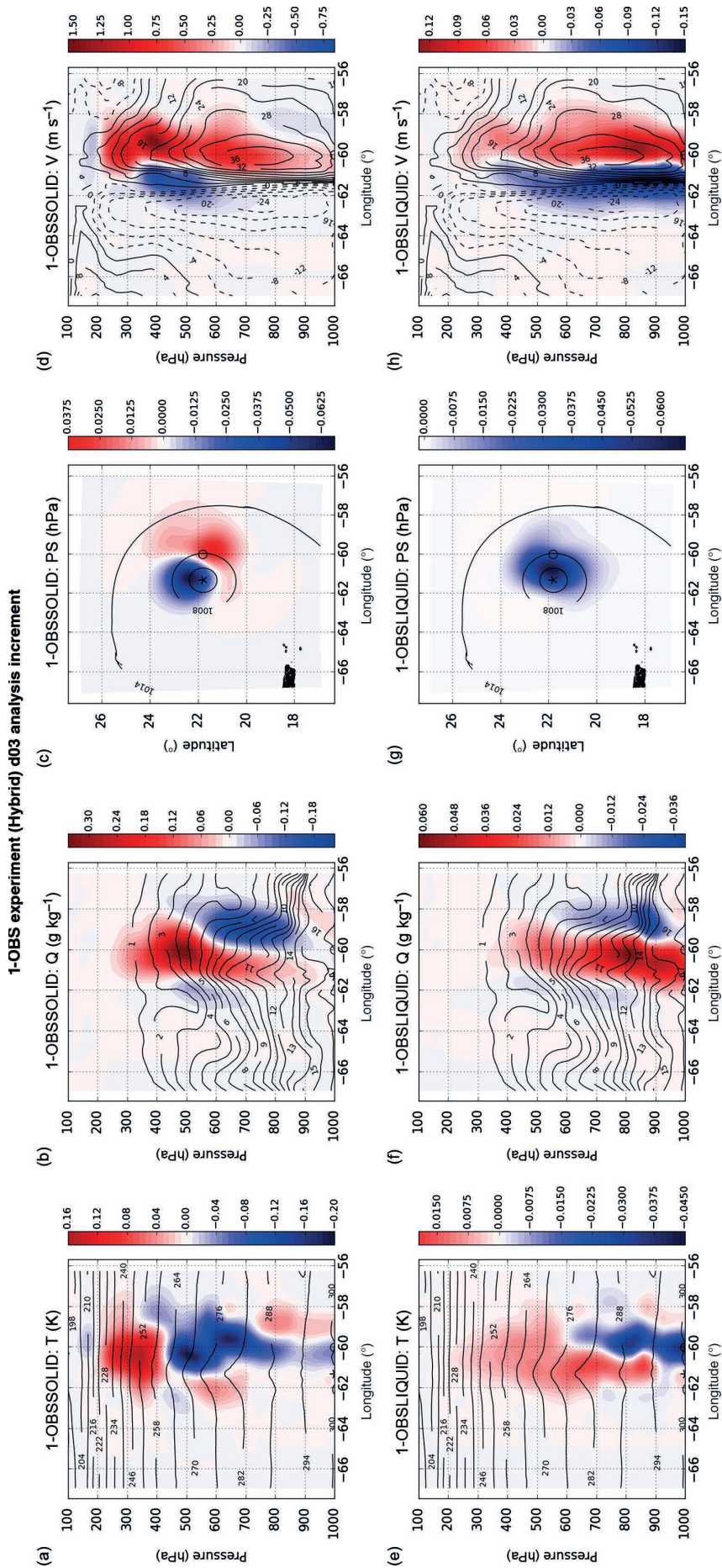


Figure 3. Same as Figure 2 except for analysis increments from the hybrid (a–d) 1-OBSOLID and (e–h) 1-OBSLIQUID experiments.

Table 3. HWRf forecast experiments for Hurricanes *Leslie* (2012) and *Gonzalo* (2014).

Experiments	1st cycle (yyyy/mm/dd hh)	2nd cycle (yyyy/mm/dd hh)
Hurricane Leslie (2012)		
L1 CTL and AddWC	2012/08/30 1800 UTC	2012/08/31 0000 UTC
Hurricane Gonzalo (2014)		
G1 CTL and AddWC	2014/10/13 0000 UTC	2014/10/13 0600 UTC
G2 CTL and AddWC	2014/10/16 0600 UTC	2014/10/16 1200 UTC

AddWC. In both L1 experiments, the first cycles begin at 1800 UTC 30 August and continue to the second cycles at 0000 UTC 31 August. Similarly, a pair of experiments is conducted during the observed developing stage of *Gonzalo* and is denoted by G1 CTL and G1 AddWC. In both G1 experiments, the first cycles begin at 0000 UTC 13 October and continue to the second cycles at 0600 UTC on the same day. During the observed mature stage of *Gonzalo*, the last pair of experiments is conducted and is denoted by G2 CTL and G2 AddWC. Likewise, in both G2 experiments, the first cycles begin at 0600 UTC 16 October and continue to the second cycles at 1200 UTC on the same day. The above-mentioned six experiments are summarized in Table 3.

Since the main difference between the CTL and AddWC experiments occur in the innermost domain, a discussion of the performance of the subsequent analysis from the second cycles of the six experiments will be specific to d03.

4.3. Results from data assimilation experiments

4.3.1. Observed vs. simulated integrated SWC and LWC

In general, background guessed values of the observed quantities are lower, potentially suggesting a negative bias due to the observation operators. An example of the observed integrated SWC and LWC that are assimilated in ghost d03 in the L1 AddWC experiment is shown in Figure 5(a) and (b). The background guessed values of integrated SWC and LWC and the counterpart from the analysis are illustrated in Figure 5(c), (d), (e) and (f), respectively. Before assimilation, the local maximum values ($\sim 2.5 \text{ kg m}^{-2}$) of the observed integrated SWC (Figure 5(a)), to the southwest quadrant of the storm (magenta star), are found to be lower in the background (Figure 5(c)). Similar remarks also apply to the integrated LWC (Figure 5(b) and (d)). By assimilating the observed integrated SWC and LWC together with the new observation operators, background guessed values of the integrated SWC and LWC are improved (Figure 5(e) and (f)) and are supported by values of the observed quantities (Figure 5(a) and (b)). When observed quantities for *Gonzalo* are assimilated into the G1 AddWC (Figure 6(a) and (b)) and G2 AddWC (Figure 7(a) and (b)) experiments, favourable results occurred in that observed quantities support the subsequent analyses. Results from L1, G1, and G2 AddWC experiments (Figures 5–7) are encouraging as they add confidence of the ability of the new observation operators (see section 3.3) that serve to modify background state into an analysis state that agrees with observations. Although there is still an indication of the potential bias, the observation innovation is considerably reduced in the analysis.

4.3.2. Differences between the CTL and AddWC analyses

As a result of the assimilation of retrieved integrated SWC and LWC in ghost d03 (AddWC experiment), the impact of the additional observations on the respective analyses (CTL vs. AddWC) is examined. Instead of taking difference between the background and analysis fields of one experiment (analysis increment, as was done in section 3.3), differences between analyses from the CTL and AddWC experiments are examined here. Due to possible asymmetries, in the azimuthal direction, a given vertical cross-section could contain information that may

Figure 4. GOES-13 visible imagery at (a) 1145 UTC 5 September 2012 during *Leslie*, and (b) 1145 UTC 16 October 2014 during *Gonzalo*.

Table 2. Experimental design for assimilating Hurricane GPROF retrieved integrated SWC and LWC in the innermost domain of HWRf. WC here denotes both integrated SWC and integrated LWC.

Experiment	Obs Assimilated in ghost d02		Obs Assimilated in ghost d03	
	Conventional	Satellite	Conventional	Satellite
CTL	✓	✓	✓	None
AddWC	✓	✓	✓	WC

Note that for all the AddWC experiments mentioned above, the observation errors assigned to integrated SWC and LWC are 1.0 and 2.0 kg m^{-2} , respectively. These two numbers are estimates of a root-mean-square deviation from all available Hurricane GPROF retrieved quantities for *Leslie* and *Gonzalo*. With this error assignment, the ratio of observation errors to the mean value of observed quantities is approximately 0.25 for integrated SWC and 0.4 for integrated LWC.

There are a total of six experiments. The first pair of experiments is conducted for *Leslie*, hereafter denoted by L1 CTL and L1

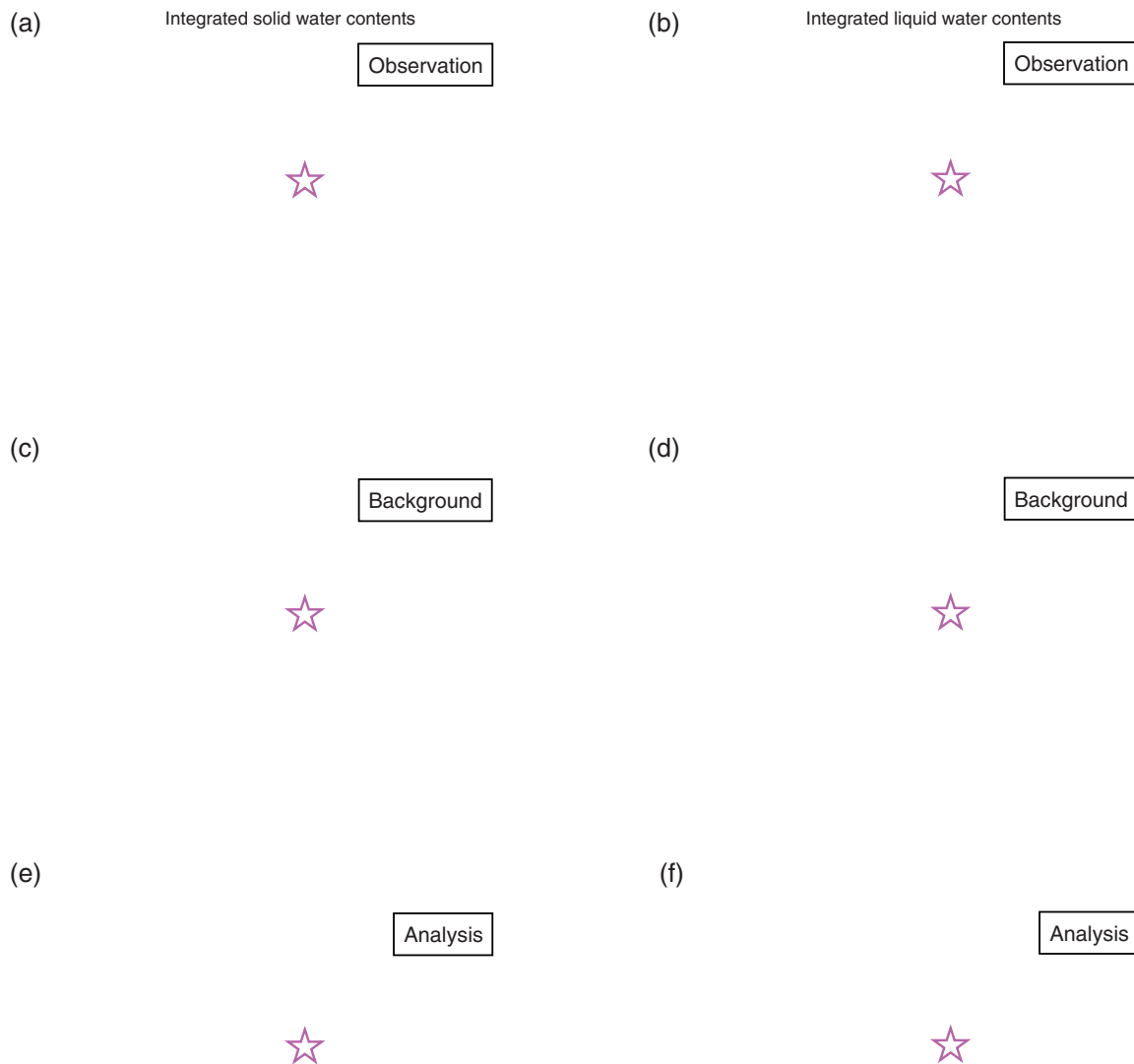


Figure 5. Hurricane GPROF retrieved (a) integrated SWC (kg m^{-2}) and (b) integrated LWC (kg m^{-2}) assimilated in the L1 AddWC experiment during *Leslie*. (c)–(d) Same as (a)–(b) except for background guessed quantities. Similarly, (e)–(f) are estimated quantities from the L1 AddWC analysis. A bold magenta star marks the centre of *Leslie* at the analysis time.

or may not be representative of the entire hurricane. To overcome this issue, azimuthally averaged quantities will be used to show differences between the two analyses, following Wu *et al.* (2014). To aid this analysis, horizontal winds in the rectilinear coordinate system (u and v) are converted to radial (V_r) and tangential (V_t) horizontal winds in a polar coordinate system centred on the hurricane.

Analyses of the L1 CTL and the L1 AddWC and the differences (L1 AddWC minus L1 CTL) are presented in Figure 8. Values of azimuthally averaged T , q , V_t and V_r from the L1 CTL analysis are shown in Figure 8(a)–(d). Likewise, Figure 8(e)–(h) show the above four variables from the L1 AddWC analysis. To examine the impact of assimilating both retrieved integrated SWC and LWC, differences between the two respective analyses are presented in Figure 8(i)–(l). In Figure 8(i), a local area of negative values of T differences between 300 and 800 hPa within the first 300 km radius suggests cooler air in the mid-tropospheric layers of the L1 AddWC analysis. Positive values of q difference (Figure 8(j)) are collocated with the negative T differences in Figure 8(i), suggesting cooler air in the mid-tropospheric layers

is accompanied by moister air. Negative values of V_t differences (Figure 8(k)) and positive values of V_r differences (Figure 8(l)) near surface and outside the first 50 km radius imply weaker rotational winds and inflows in the lower tropospheric layers of the L1 AddWC analysis. In contrast, large positive values of V_t differences (Figure 8(k)) and positive values of V_r differences (Figure 8(l)) above 300 hPa both suggest stronger rotational winds and outflows in the upper tropospheric layers of the L1 AddWC analysis. The impact of assimilating both retrieved integrated SWC and LWC in the core region of *Leslie* on the above-mentioned variables are mixed. Thus, physical interpretations are precluded. In general, moister and cooler air in the near-core region is evident in the mid-tropospheric layers of the L1 AddWC analysis, suggesting a favourable environment for saturation. Slightly weaker winds in lower, but much stronger upper-layer rotational winds and outflows are also evident in the L1 AddWC analysis.

Similar to Figure 8, azimuthally averaged quantities from the G1 CTL and G1 AddWC analyses and the difference fields are shown in Figure 9. While responses to T are mixed (Figure 9(i)), moister

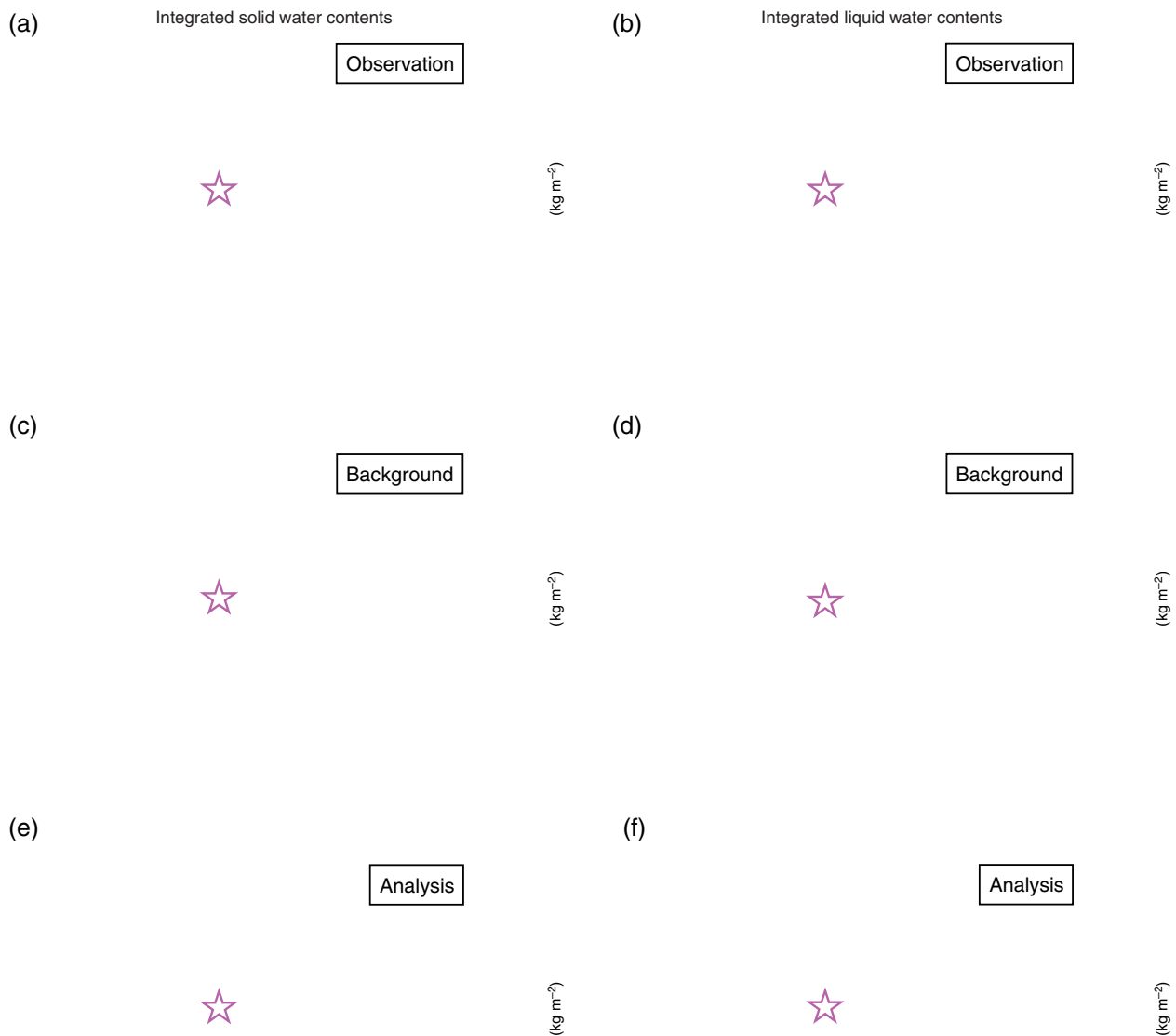


Figure 6. Same as Figure 5, except for retrieved quantities that are assimilated in the G1 AddWC experiment during *Gonzalo*.

air throughout the vertical column within the first 100 km radius is evident in the G1 AddWC analysis (Figure 9(j)). In Figure 9(k) and (l), V_r and V_r differences both suggest the G1 AddWC analysis has slightly stronger rotational winds throughout the vertical, and also greater inflows in the lower layer and greater outflows in the upper layer compared to the G1 CTL analysis. In general, large spatial variability in the difference fields is evident. Such a response is expected due to the mixed impact from assimilating both retrieved integrated SWC and LWC with the hybrid option (i.e. the operational configuration of GSI in HWRF). Like the 1-OBS hybrid experiments, physical interpretation of analysis differences is challenging. Since our cases are hurricanes, one approach could be to examine the hydrostatic linking of warmer temperatures aloft with lower surface pressures (as was described in section 3.4) to larger tangential wind speeds through gradient wind balance. However, for the simulations presented herein, azimuthally averaging (e.g. Figures 8 and 9) removes asymmetries that are present in the three-dimensional analysis fields. For brevity, conclusions from the G2 experiments are similar to G1.

Overall, results from the six experiments are encouraging. By assimilating additional observations in ghost d03 (AddWC experiments), background guessed values of the integrated SWC

and LWC are adjusted to an analysis state that is supported by observed quantities. In general, the impact of assimilating both retrieved integrated water contents causes moister and cooler air in the mid-tropospheric layers to approach saturation when background guess values are lower (e.g. Figures 5–7). While responses to the winds are mixed, results indicated increased rotational and radial winds in the upper layers.

5. HWRF forecast

A variety of metrics will be used to examine the impact of assimilating Hurricane GPROF data on HWRF forecasts. To begin with, hurricane track, size,⁹ and intensity of six forecasts are computed by using the GFDL vortex tracker (Marchok, 2002) package embedded in HWRF. These metrics are then compared with the NHC best-track data. Also, simulated precipitation

⁹Hurricane size is often described by the maximum extent of winds of 34, 50 and 64 kn in each of quadrants about the centre (Landsea and Franklin, 2013). In this study, quadrant-averaged 34 kn wind radius is used as an approximation of hurricane size.



Figure 7. Same as Figure 6, but for retrieved quantities that are assimilated in the G2 AddWC experiment during *Gonzalo*.

fields from all six forecasts are compared with rain rates from the TRMM and GPM instruments. Finally, synthetic GOES-13 images generated from all six forecasts (using a version of the Community Radiative Transfer Model (CRTM) external to HWRP) are compared with observed GOES-13 images (e.g. Grasso *et al.*, 2014).

5.1. Hurricane track, size, and intensity

Hurricane track, size, minimum central sea-level pressure (MSLP), and maximum 10 m winds (WMAX) from two 126 h HWRP forecasts that are initialized with L1 CTL (blue line) and L1 AddWC (green line) analyses are presented in Figure 10. Results show that there is no obvious difference between track forecasts from L1 CTL and L1 AddWC (Figure 10(a)). On the other hand, both L1 CTL and L1 AddWC forecasts generate larger storms (~100 km larger than the NHC best-track data), and remain larger than the NHC (black line) estimated sizes for the first 36 h (Figure 10(b)). Similarly, the intensity as measured by MSLP and WMAX of the simulated storms from the L1 CTL and the L1 AddWC forecasts produce more intense storms than the NHC estimates (Figure 10(c) and (d)). Note in particular that the L1

AddWC forecast, however, intensifies the simulated hurricane after the first 72 h and is much different from the L1 CTL forecast.

Figure 11 shows results from the G1 CTL (blue line) and the G1 AddWC (green line) forecasts. Similar to the L1 *Leslie* forecasts, Figure 11(a) exhibits no obvious distinction between the G1 CTL and the G1 AddWC track forecasts. In this case, the simulated storm sizes from both forecasts are found to be comparable to the NHC estimated sizes (black line) in the first 18 h of the forecasts (Figure 11(b)). However, the difference in sizes between both G1 forecasts and the NHC estimated sizes is nearly constant with a value of ~20 km, indicating slightly larger storm sizes in both forecasts. Unlike the L1 forecasts, values of MSLP and WMAX (Figure 11(c) and (d)) suggest both G1 CTL and G1 AddWC forecasts underestimate the intensity of *Gonzalo* when compared to the NHC estimates throughout the 126 h period. It is noteworthy that the G1 AddWC intensity forecast is generally better than the G1 CTL intensity forecast.

As for the last pair of forecasts, results from the G2 CTL and G2 AddWC are presented in Figure 12. Both track and size comparisons from the G2 CTL and G2 AddWC forecasts exhibit similarities to the previous two pairs of forecasts (Figure 12(a) and (b)). Unlike the L1 and G1 pairs of forecasts, the G2 pair of

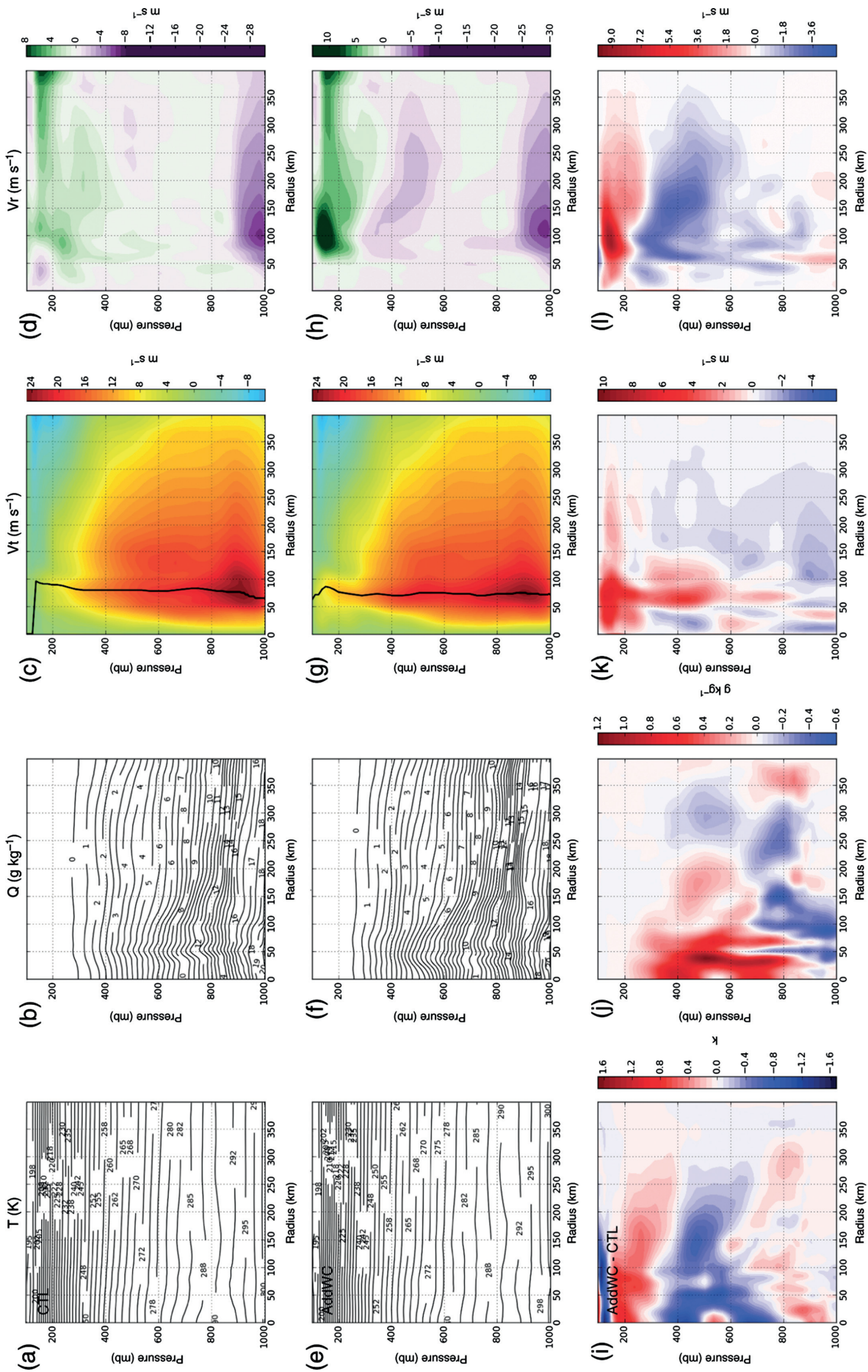


Figure 8. Vertical profiles of azimuthally averaged (a) temperature (K), (b) specific humidity (g kg^{-1}), (c) tangential winds (m s^{-1}) and the radius of maximum winds (RMW, black contour), and (d) radial winds (m s^{-1}) from the L1 CTL analysis during *Leslie*. (e)–(h) Same as (a)–(d) except for the L1 AddWC analysis. (i)–(l) are differences between the L1 CTL and the L1 AddWC analyses (L1 AddWC minus L1 CTL).

D03 AzMean initialized at 2014101306

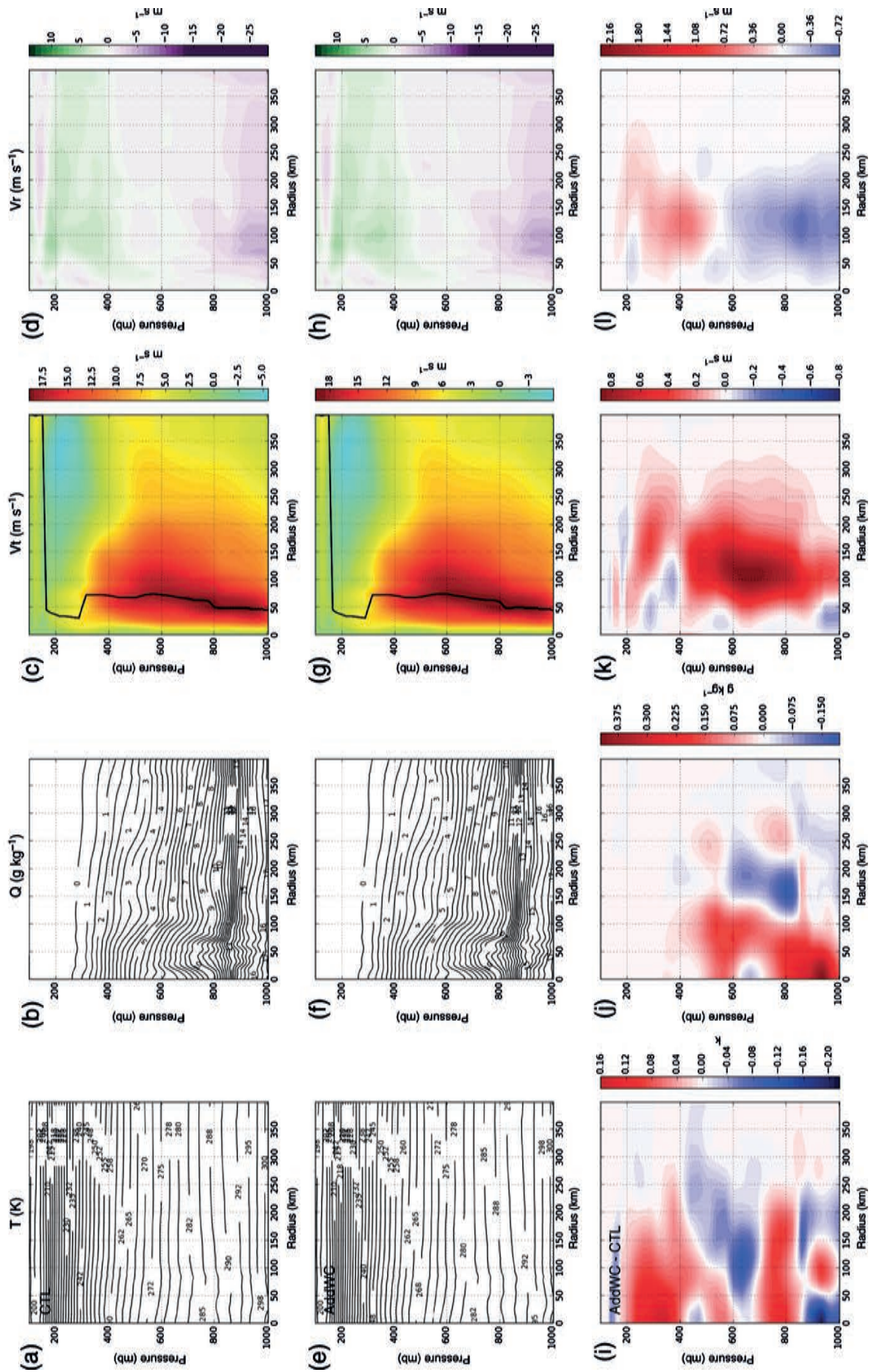


Figure 9. Same as Figure 8, except for the G1 CTL and the G1 AddWC analyses during *Gonzalo*.

Figure 10. The 126 h HWRF forecast (a) track (km), (b) size (km), (c) minimum mean sea-level pressure (hPa), and (d) maximum 10 m winds (kt) initialized from the L1 CTL (blue) and the L1 AddWC (green) analyses during *Leslie*. Black solid lines represent the corresponding estimates from NHC best-track data.

forecasts is initialized at a time when *Gonzalo* was a hurricane and covers the time period when the system underwent continuous weakening, underwent extratropical transition (completed on 19 October 1800 UTC, 78 h), and eventually dissipated. In Figure 12(c) and (d), the G2 CTL and G2 AddWC forecasts of MSLP are found to be quite similar to the NHC estimated intensity for the first 48 h. In the rest of the forecast period, MSLP forecasts from both G2 CTL and G2 AddWC exhibit relatively large deviation from the NHC estimates during the period of extratropical transition; however, the corresponding WMAX forecasts are rather similar to the NHC estimated quantities.

5.2. Precipitation

Simulated precipitation fields from all six forecasts are compared with rain rates from TRMM and GPM instruments. For this study, footprint sizes of instantaneous rain rates (mm h^{-1}) from TRMM at nadir are $\sim 30 \times 20 \text{ km}^2$ and $\sim 4.3 \text{ km}$ for TMI and PR, respectively. Similarly, footprint sizes of instantaneous rain rates (mm h^{-1}) from GPM at nadir are $\sim 16 \times 10 \text{ km}^2$ and $\sim 5 \text{ km}$ for GMI and DPR, respectively. In addition, d03 is small enough that the hurricane rain bands extend beyond the boundary of the innermost domain; consequently, simulated and observed rain rates will be displayed in d02. Due to the footprint sizes of rain rate data from TRMM/GPM, a comparison of patterns near the cumulus scale is avoided in favour of a qualitative comparison of patterns on a larger scale.

Although instantaneous rain rates are unavailable from HWRF, other output variables are used to compare with TRMM/GPM. One such variable is CWM. Following Zhang *et al.* (2013a),

CWM is integrated over the depth of the simulated domain and is displayed in Figure 13.

Rain rates from TMI/PR that are valid at 1800 UTC 31 August 2012 are compared to the column-integrated CWM field (kg m^{-2} ; equivalent to mm) from the L1 CTL and the L1 AddWC 18 h forecasts (Figure 13(a)–(c)). Like observations (Figure 13(a)), the majority of the precipitation field is to the south of the centre of *Leslie* (bold star) in both the L1 CTL (Figure 13(b)) and the L1 AddWC (Figure 13(c)) forecasts. Larger values of column-integrated CWM to the south of the simulated systems are reminiscent of convective activity that advects cyclonically around the centre. Similar to the L1 forecasts, the simulated rain rates from both G1 forecasts exhibit larger values to the northeast of the centre of *Gonzalo* (bold star) and are supported by observed rain rates from GMI/DPR (Figure 13(d)–(f)). Unlike the spatial patterns exhibited in Figure 13(a)–(f), the regions of simulated rain rates encircle the centre of *Gonzalo* (bold star) in both observed and simulated fields (Figure 13(g)–(i)). Similar comparisons between simulated rain rates from HWRF forecasts and retrieved rain rates from the Advanced Microwave Sounding Unit were also examined and showed similar results, but are not shown for the sake of brevity.

5.3. Synthetic satellite images

Due to the lack of available observations over oceans, TRMM/GPM rain rates are supplemented with GOES-13 images. One way to use observed GOES-13 images is through the use of satellite images generated from HWRF outputs (referred to as synthetic satellite images). Synthetic satellite images (Bikos *et al.*, 2012) for all six forecasts are shown along with observed

Figure 11. Same as Figure 10, except for HWRF forecasts initialized from the G1 CTL and the G1 AddWC analyses during *Gonzalo*.

Figure 12. Same as Figure 11, except for HWRF forecasts initialized from the G2 CTL and the G2 AddWC analyses during *Gonzalo*.

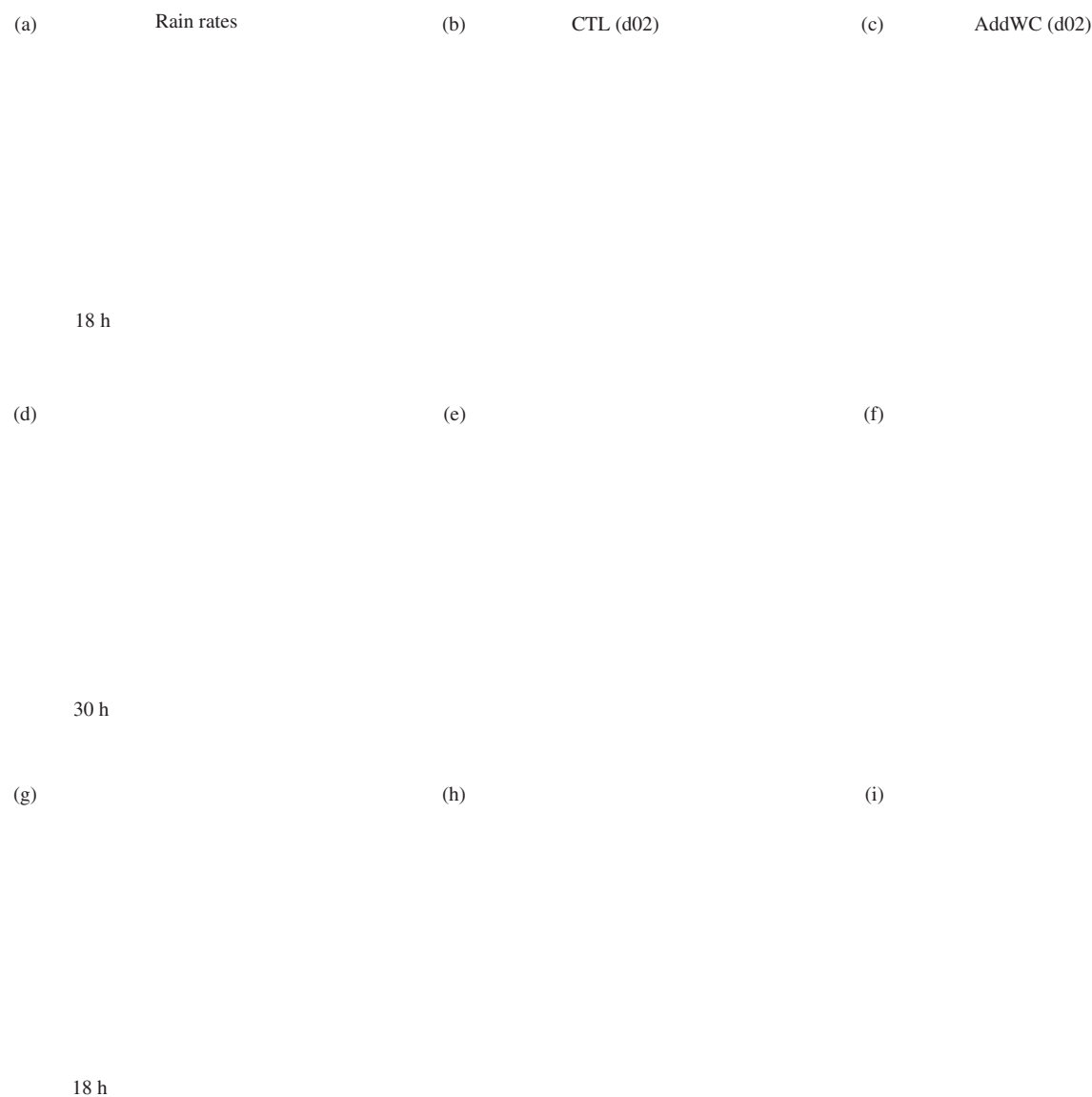


Figure 13. (a) PR measured (within black lines) and TMI estimated (outside black lines) rain rates (mm h^{-1} in log scale) and column-integrated CWM (kg m^{-2} in log scale) from 18 h HWRf forecasts that are initialized from (b) the L1 CTL and (c) the L1 AddWC analyses during *Leslie*. (d) DPR measured (within black lines) and GMI estimated (outside black lines) rain rates (mm h^{-1} in log scale). (e)–(f) Same as (b)–(c), except for 30 h HWRf forecasts that are initialized from the G1 CTL and the G1 AddWC analyses during *Gonzalo*. Similarly, (g)–(i) are results from 18 h HWRf forecasts that are initialized from the G2 CTL and the G2 AddWC analyses during *Gonzalo*. A bold magenta star marks hurricane centre. The unit kg m^{-2} is equivalent to mm after dividing by density of liquid water, which is 1000 kg m^{-3} .

GOES-13 images at $10.7 \mu\text{m}$ (Figure 14). In the figure, observed and synthetic GOES-13 imagery from the L1 CTL and the L1 AddWC forecasts are shown in Figure 14(a)–(c); imagery from the G1 CTL and the G1 AddWC forecasts are exhibited in Figure 14(d)–(f); and results from the final pair are displayed in Figure 14(g)–(i). All synthetic images are generated with the CRTM and brightness temperatures are sensitive to particle sizes. For this study, the particle size of ice is set to $75 \mu\text{m}$, a size that is consistent with particle sizes of ice in GSI.

In general, the area within the dash boxes of the synthetic images that is occupied by cold clouds ($< -60^\circ\text{C}$) is larger than the corresponding area in the observed images. These cold biases are particularly evident in the coldest cloud tops with HWRf forecasts having nearly twice as much area being covered by cloud tops colder than -70°C . It is interesting to note that as the temperature threshold is increased to -40°C the areal coverage in HWRf is more comparable and actually slightly smaller than the observations. This may be suggesting that the convective vertical motions are overactive in HWRf or other issues related to microphysics. Additionally, these findings are consistent with observational studies relating infrared imagery to tropical cyclone wind structures (Knaff *et al.*, 2014, 2016) and the

results presented in section 5.1, in which a larger and more intense tropical system is found in both L1 CTL and L1 AddWC forecasts. Finally, it is also noteworthy that the assimilation of retrieved integrated SWC and LWC from TRMM/GPM provides slightly improved initial conditions in terms of the observed GOES-13 imagery.

6. Summary and discussion

The GSI capability of assimilating satellite-retrieved integrated SWC and LWC from Hurricane GPROF in HWRf is developed and assessed in this study. To assimilate the retrieved integrated water contents, new observation operators are developed and implemented in GSI. The concept behind the development of the new observation operators assumes all water vapour in excess of saturation with respect to ice or liquid will be immediately condensed out. Without introducing new control variables into GSI, the new observation operators are implemented in such a way that the information of integrated water contents is extended to some – temperature, specific humidity and pressure – of the current set of GSI control variables.

Figure 14. (a) GOES-13 10.7 μm infrared imagery and the corresponding synthetic satellite images (brightness temperature in $^{\circ}\text{C}$) from 6 h HWRF forecasts that are initialized from (b) the L1 CTL and (c) the L1 AddWC analyses during *Leslie*. Regions of interest, d03 of HWRF, are shown in the dash box. (d)–(f) Same as (a)–(c) except for 6 h HWRF forecasts that are initialized from the G1 CTL and the G1 AddWC analyses during *Gonzalo*. Similarly, (g)–(i) are results from 6 h HWRF forecasts that are initialized from the G2 CTL and the G2 AddCW analyses during *Gonzalo*. A bold magenta star marks hurricane centre in the GOES-13 image.

Two 1-OBS experiments that use the no-hybrid option are conducted to assimilate a single integrated SWC and a single integrated LWC both of which are for a hurricane environment. Both no-hybrid experiments suggest that the new observation operators are capable of extending information from integrated SWC and integrated LWC into nearby grid points and other state variables in a physically consistent way. In particular, a concise physical interpretation is provided to explain analysis increments in temperature, specific humidity and surface pressure from the no-hybrid 1-OBS experiments. Results from the corresponding experiments that are conducted with a hybrid option exhibit more spatial variability because of the inclusion of flow-dependent background error covariance that originates from GFS ensemble forecasts. Due to the variability in the hybrid 1-OBS experiments, a physical interpretation is less straightforward. Nevertheless, analysis increments from the above-mentioned state variables exhibit consistent adjustment from a background state to an analysis.

Two hurricanes, *Leslie* (2012) and *Gonzalo* (2014), are selected to perform three sets of two data assimilation experiments with the use of the retrieved integrated SWC and LWC within HWRF. A CTL experiment, following the current operational HWRF implementation, and an AddWC experiment that assimilates

Hurricane GPROF retrieved integrated SWC and LWC together along with conventional observations in the innermost domain are conducted. In general, moister and cooler air in mid to lower tropospheric layers of the hurricane core are evident in the AddWC analysis, suggesting a tendency toward reaching saturation by lowering temperature and increasing moisture. Tangential and radial winds resolved in the AddWC analysis are slightly more intense in the mid to upper tropospheric layers, near the hurricane core, compared to the CTL analysis.

Although ‘all water vapour in excess of the saturation is immediately condensed out’ is a valid assumption, the model microphysics and/or cumulus parametrization has already condensed out a portion of supersaturated water vapour. As a result, the supersaturation computed by the observation operators is likely reduced, therefore potentially creating a negative bias of the guess. A possible remedy for this issue will be to introduce/add a model variable in HWRF to retain an adequate amount of excessive water vapour. Nevertheless, the results indicate that the system is still able to considerably reduce the observation innovation in the analysis.

In general, the impact of assimilating the TRMM/GPM precipitation observations (integrated SWC and integrated LWC) in the innermost domain on the HWRF forecasts is inconclusive.

Both the CTL and the AddWC forecasts generate larger hurricanes compared to observations. However, the impact on the AddWC forecasts was to produce lower MSLP and greater WMAX at times. Comparisons between both the CTL and the AddWC forecasts to TRMM/GPM rain rates suggest that the simulated precipitation fields are not only similar between the two forecasts, but also comparable to observations. The synthetic satellite images generated from the CTL and the AddWC forecasts exhibit similar characteristics. However, issues in the synthetic images are identified from a comparison between synthetic and observed GOES-13 images. These issues include (i) colder cloud-top brightness temperatures and (ii) larger spatial extension of cold brightness temperatures, both in the vicinity of the simulated tropical storms. A few possible causes of the inconclusive nature of our results are the following: (i) the analysis used to initialize an HWRF forecast is unbalanced, (ii) the existence of forecast model errors (e.g. errors in microphysics parametrization schemes) that are not accounted for by the HWRF data assimilation system, and (iii) the absence of hydrometeor variables in the list of operational GSI control variables.

A few different approaches will be explored in future work. In this study, a retrieved quantity was assimilated and the impact on HWRF forecasts was inconclusive. A statistical inference about the impact on the general population of experiments where retrieved precipitation observations are assimilated into HWRF requires more experiments than the two presented here (i.e. sample size is too small). Long-term efforts will extend current work by conducting similar experiments with more hurricane cases and also explore the feasibility of assimilating all-sky satellite radiances directly into HWRF.

Acknowledgements

This research is primarily funded by NOAA's Sandy Supplemental Award NA14OAR4830122. We would like to acknowledge the high-performance computing support from Yellowstone provided by NCAR's Computational and Information Systems Laboratory, sponsored by the National Science Foundation. The views, opinions, and findings in this report are those of the authors, and should not be construed as an official NOAA and/or US Government position, policy, or decision. The authors are grateful to the two anonymous reviewers for their careful reviews and valuable comments.

Appendix

Jacobians for integrated SWC and integrated LWC operators

The derivatives of the integrated SWC and/or integrated LWC operator with respect to T , P and q , also known as Jacobians, are also calculated. From Eqs (1)–(9), the operator at each model vertical level k can be rewritten as

$$h^k = \left\{ \left(\frac{q^k}{1-q^k} \right) - 0.622 \frac{e_s(T^k)}{P^k - e_s(T^k)} \right\} \rho^k \Delta z^k \quad (\text{A1})$$

using the same notations. Since $\rho^k \Delta z^k$ is equivalent to $\frac{\Delta P^k}{g}$ according to the hydrostatic equation and ideal gas law, Eq. (A1) can be written as

$$h^k = \left\{ \left(\frac{q^k}{1-q^k} \right) - 0.622 \frac{e_s(T^k)}{P^k - e_s(T^k)} \right\} \frac{\Delta P^k}{g}. \quad (\text{A2})$$

For simplicity, the vertical index k is dropped, and the operator at each model vertical level can then be expressed by

$$h = \left\{ \left(\frac{q}{1-q} \right) - 0.622 \frac{e_s(T)}{P - e_s(T)} \right\} \frac{\Delta P}{g} \quad (\text{A3})$$

as a function of T , P and q : $h = f(T, P, q)$.

The corresponding tangent linear and adjoint operators are a linear combination of perturbations of T , P and q :

$$\delta h = \frac{\partial h}{\partial T} \delta T + \frac{\partial h}{\partial P} \delta P + \frac{\partial h}{\partial q} \delta q, \quad (\text{A4})$$

where δh represents the increments of integrated SWC or integrated LWC, and δT , δP and δq are the perturbations of T , P and q , respectively. Similarly, $\frac{\partial h}{\partial T}$, $\frac{\partial h}{\partial P}$ and $\frac{\partial h}{\partial q}$ are the Jacobians with respect to T , P and q . Based on the approximate calculation of derivatives of $\frac{\Delta P}{g}$ with respect to T , P and q , it is assumed that these derivatives are negligible compared to the derivatives of $\left(\frac{q}{1-q} \right) - 0.622 \frac{e_s(T)}{P - e_s(T)}$ with respect to T , P and q . The Jacobians can then be written as below:

$$\frac{\partial h}{\partial T} = -0.622 \frac{P}{(P - e_s)^2} \frac{\partial e_s}{\partial T} \frac{\Delta P}{g}, \quad (\text{A5a})$$

$$\frac{\partial h}{\partial P} = 0.622 \frac{e_s}{(P - e_s)^2} \frac{\Delta P}{g}, \quad (\text{A5b})$$

$$\frac{\partial h}{\partial q} = \frac{1}{(1-q)^2} \frac{\Delta P}{g}. \quad (\text{A5c})$$

In Eq. (A5a),

$$\frac{\partial e_s}{\partial T} = e_{sl} \frac{\partial w}{\partial T} + w \frac{\partial e_{sl}}{\partial T} - e_{si} \frac{\partial w}{\partial T} + (1-w) \frac{\partial e_{si}}{\partial T}, \quad (\text{A6})$$

where

$$\frac{\partial w}{\partial T} = 2 \frac{1}{\cosh^2(\Delta T)} \left(\frac{1}{T_0 - T_{\text{mix}}} \right), \quad (\text{A7})$$

$$\frac{\partial e_{sl}}{\partial T} = e_{sl} \left(\frac{-C_1^{\text{liquid}}}{T} + C_2^{\text{liquid}} \cdot \frac{T_0}{T^2} \right), \quad (\text{A8})$$

and

$$\frac{\partial e_{si}}{\partial T} = e_{si} \left(\frac{-C_1^{\text{ice}}}{T} + C_2^{\text{ice}} \cdot \frac{T_0}{T^2} \right). \quad (\text{A9})$$

The above equations are implemented in GSI.

References

- Bernardet L, Tallapragada V, Bao S, Trahan S, Kwon Y, Liu Q, Tong M, Biswas M, Brown T, Stark D, Carson L, Yablonsky R, Uhlhorn E, Gopalakrishnan S, Zhang X, Marchok T, Kuo B, Gall R. 2015. Community support and transition of research to operations for the Hurricane Weather Research and Forecasting model. *Bull. Am. Meteorol. Soc.* **96**: 953–960, doi: 10.1175/BAMS-D-13-00093.1.
- Bikos D, Lindsey DT, Otkin J, Sieglaff J, Grasso L, Siewart C, Correia J, Coniglio M, Rabin R, Kain JS, Dembek S. 2012. Synthetic satellite imagery for real-time high-resolution model evaluation. *Weather and Forecasting* **27**: 784–795, doi: 10.1175/WAF-D-11-00130.1.
- Brown DP. 2015. 'Hurricane Gonzalo (AL082014): 12–19 October 2014', National Hurricane Center Tropical Cyclone report. www.nhc.noaa.gov/data/tcr/AL082014_Gonzalo.pdf (accessed 15 August 2016).
- Brown PJ, Kummerow CD, Randel DL. 2016. Hurricane GPROF: An optimized ocean microwave rainfall retrieval for tropical cyclones. *J. Atmos. Oceanic Technol.* **33**: 1539–1556, doi: 10.1175/JTECH-D-15-0234.1.
- Chambon P, Zhang SQ, Hou AY, Zupanski M, Cheung S. 2014. Assessing the impact of pre-GPM microwave precipitation observations in the Goddard WRF ensemble data assimilation system. *Q. J. R. Meteorol. Soc.* **140**: 1219–1235, doi: 10.1002/qj.2215.
- Cotton WR. 1972. Numerical simulation of precipitation development in supercooled cumuli – Part II. *Mon. Weather Rev.* **100**: 764–784, doi: 10.1175/1520-0493(1972)100<0764:NSOPDI>2.3.CO;2.

- Emanuel KA. 1994. *Atmospheric Convection*. Oxford University Press: New York, NY.
- Ferrier BS. 2005. An efficient mixed-phase cloud and precipitation scheme for use in operational NWP models. *Eos. Trans. Am. Geophys. Union* **86** Jt. Assem. Suppl.: A42A02.
- Grasso L, Lindsey DT, Lim K-SS, Clark A, Bikos D, Dembek SR. 2014. Evaluation of and suggested improvements to the WSM6 microphysics in WRF-ARW using synthetic and observed GOES-13 imagery. *Mon. Weather Rev.* **142**: 3635–3650, doi: 10.1175/MWR-D-14-00005.1.
- Hence DA, Houze RA Jr. 2012. Vertical structure of tropical cyclone rainbands as seen by the TRMM precipitation radar. *J. Atmos. Sci.* **69**: 2644–2661, doi: 10.1175/JAS-D-11-0323.1.
- Hou AY, Zhang SQ, Reale O. 2004. Variational continuous assimilation of TMI and SSM/I rain rates: Impact on GEOS-3 hurricane analyses and forecasts. *Mon. Weather Rev.* **132**: 2094–2109, doi: 10.1175/1520-0493(2004)132<2094:VCAOTA>2.0.CO;2.
- Hou AY, Kakar RK, Neeck S, Azarbarzin AA, Kummerow CD, Kojima M, Oki R, Nakamura K, Iguchi T. 2014. The global precipitation measurement mission. *Bull. Am. Meteorol. Soc.* **95**: 701–722, doi: 10.1175/BAMS-D-13-01064.1.
- Iguchi T, Kozu T, Meneghini R, Awaka J, Okamoto K. 2000. Rain-profiling algorithm for the TRMM precipitation radar. *J. Appl. Meteorol.* **39**: 2038–2052, doi: 10.1175/1520-0450(2001)040<2038:RPAFTT>2.0.CO;2.
- Janjic ZI. 2003. A nonhydrostatic model based on a new approach. *Meteorol. Atmos. Phys.* **82**: 271–285, doi: 10.1007/s00703-001-0587-6.
- Kleist DT, Parrish DF, Derber JC, Treadon R, Wu W-S, Lord S. 2009. Introduction of the GSI into the NCEP Global Data Assimilation System. *Weather Forecasting* **24**: 1691–1705, doi: 10.1175/2009WAF2222201.1.
- Knaff JA, Longmore SP, Molenaar DA. 2014. An objective satellite-based tropical cyclone size climatology. *J. Clim.* **27**: 455–476, doi: 10.1175/JCLI-D-13-00096.1.
- Knaff JA, Slocum CJ, Musgrave KD, Sampson CR, Strahl BR. 2016. Using routinely available information to estimate tropical cyclone wind structure. *Mon. Weather Rev.* **144**: 1233–1247, doi: 10.1175/MWR-D-15-0267.1.
- Kumar P, Kishtawal CM, Pal PK. 2014. Impact of satellite rainfall assimilation on Weather Research and Forecasting model predictions over the Indian region. *J. Geophys. Res. Atmos.* **119**: 2017–2031, doi: 10.1002/2013JD020005.
- Kummerow CD, Barnes W, Kozu T, Shiue J, Simpson J. 1998. The Tropical Rainfall Measuring Mission (TRMM) sensor package. *J. Atmos. Oceanic Technol.* **15**: 809–817, doi: 10.1175/1520-0426(1998)015<0809:TTRMMT>2.0.CO;2.
- Kummerow CD, Hong Y, Olson WS, Yang S, Adler RF, McCollum J, Ferraro R, Petty G, Shin D-B, Wilhelm TT. 2001. The evolution of the Goddard Profiling algorithm (GPROF) for rainfall estimation from passive microwave sensors. *J. Appl. Meteorol.* **40**: 1801–1820, doi: 10.1175/1520-0450(2001)040<1801:TEOTGP>2.0.CO;2.
- Kummerow CD, Randel DL, Kulie M, Wang N-Y, Ferraro R, Munchak SJ, Petkovic V. 2015. The evolution of the Goddard Profiling algorithm to a fully parametric scheme. *J. Atmos. Oceanic Technol.* **32**: 2265–2280, doi: 10.1175/JTECH-D-15-0039.1.
- Landsea CW, Franklin JL. 2013. Atlantic hurricane database uncertainty and presentation of a new database format. *Mon. Weather Rev.* **141**: 3576–3592, doi: 10.1175/MWR-D-12-00254.1.
- Lorenz AC, Rawlins F. 2005. Why does 4D-Var beat 3D-Var? *Q. J. R. Meteorol. Soc.* **131**: 3247–3257, doi: 10.1256/qj.05.85.
- Marchok TP. 2002. 'How the NCEP tropical cyclone tracker works'. In *Preprints, 25th Conference on Hurricanes and Tropical Meteorology*, American Meteorological Society, San Diego, CA, pp. 21–22.
- Morrison H, Curry JA, Shupe MD, Zuidema P. 2005. A new double-moment microphysics parameterization for application in cloud and climate models. Part II: Single-column modeling of Arctic clouds. *J. Atmos. Sci.* **62**: 1678–1693, doi: 10.1175/JAS3447.1.
- National Oceanic and Atmospheric Administration. 2010. 'NOAA's next generation strategic plan, 2009–2014'. <http://www.ppi.noaa.gov/ngsp/> (accessed 15 August 2016).
- Parrish DF, Derber JC. 1992. The National Meteorological Center's spectral statistical-interpolation analysis system. *Mon. Weather Rev.* **120**: 1747–1763, doi: 10.1175/1520-0493(1992)120<1747:TSMCSS>2.0.CO;2.
- Pu ZX, Tao W-K, Braun S, Simpson J, Jia YQ, Halverson J, Olson W, Hou A. 2002. The impact of TRMM data on mesoscale numerical simulation of Supertyphoon *Paka*. *Mon. Weather Rev.* **130**: 2448–2458.
- Purser RJ, Wu W-S, Parrish DF, Roberts NM. 2003. Numerical aspects of the application of recursive filters to variational statistical analysis. Part I: Spatially homogeneous and isotropic Gaussian covariances. *Mon. Weather Rev.* **131**: 1524–1535, doi: 10.1175/1520-0493(2003)131<1524:NAOTAO>2.0.CO;2.
- Rappaport EN, Franklin JL, Avila LA, Baig SR, Beven JL, Blake ES, Burr CA, Jiing J-G, Juckins CA, Knabb RD, Landsea CW, Mainelli M, Mayfield M, McAdie CJ, Pasch RJ, Sisko C, Stewart SR, Tribble AN. 2009. Advances and challenges at the National Hurricane Center. *Weather and Forecasting* **24**: 395–419, doi: 10.1175/2008WAF2222128.1.
- Simpson J, Kummerow CD, Tao W-K, Adler RF. 1996. On the tropical rainfall measuring mission (TRMM). *Meteorol. Atmos. Phys.* **60**: 19–36, doi: 10.1007/BF01029783.
- Stewart SR. 2013. Hurricane *Leslie* (AL122012) 30 August – 11 September 2012. Tropical Cyclone report. National Hurricane Center: Miami, FL. http://www.nhc.noaa.gov/data/tcr/AL122012_Leslie.pdf (accessed 15 August 2016).
- Tallapragada V, Bernadet L, Biswas MK, Gopalakrishnan S, Kwon Y, Liu Q, Marchok T, Sheinin D, Thomas B, Tong M, Trahan S, Tuleya R, Yablonsky R, Zhang X. 2014. *Hurricane Weather Research and Forecasting (HWRF) Model: 2014 Scientific Documentation*. Developmental Testbed Center: Boulder, CO.
- Tallapragada V, Bernadet L, Biswas MK, Ginis I, Kwon Y, Liu Q, Marchok T, Sheinin D, Thomas B, Tong M, Trahan S, Wang W, Yablonsky R, Zhang X. 2015. 'Hurricane Weather Research and Forecasting (HWRF) Model: 2015 scientific documentation', NCAR Technical Note NCAR/TN-522+STR. NCAR/UCAR: Boulder, CO. <http://nldr.library.ucar.edu/collections/technotes/TECH-NOTE-000-000-000-893.pdf> (accessed 15 August 2016).
- Thompson G, Rasmussen RM, Manning K. 2004. Explicit forecasts of winter precipitation using an improved bulk microphysics scheme. Part I: Description and sensitivity analysis. *Mon. Weather Rev.* **132**: 519–542, doi: 10.1175/1520-0493(2004)132<0519:EFOWPU>2.0.CO;2.
- Wang X. 2010. Incorporating ensemble covariance in the Gridpoint Statistical Interpolation variational minimization: a mathematical framework. *Mon. Weather Rev.* **138**: 2990–2995, doi: 10.1175/2010MWR3245.1.
- Wu W-S, Purser RJ, Parrish DF. 2002. Three-dimensional variational analysis with spatially inhomogeneous covariances. *Mon. Weather Rev.* **130**: 2905–2916, doi: 10.1175/1520-0493(2002)130<2905:TDDVAWS>2.0.CO;2.
- Wu T-C, Liu H, Majumdar SJ, Velden CS, Anderson JL. 2014. Influence of assimilating satellite-derived atmospheric motion vector observations on numerical analyses and forecasts of tropical cyclone track and intensity. *Mon. Weather Rev.* **142**: 49–71, doi: 10.1175/MWR-D-13-00023.1.
- Yablonsky RM, Ginis I, Thomas B, Tallapragada V, Sheinin D, Bernadet L. 2015. Description and analysis of the ocean component of NOAA's operational Hurricane Weather Research and Forecasting model (HWRF). *J. Atmos. Oceanic Technol.* **32**: 144–163, doi: 10.1175/JTECH-D-14-00063.1.
- Yu H, Marchok T, Woo W-C. 2014. 'Topic 8: Rainfall'. In *WMO's Third International Workshop on Tropical Cyclone Landfall Processes*, 8–10 December 2014. Jeju, Republic of Korea. http://www.wmo.int/pages/prog/arep/wwrp/new/documents/C_T8.pdf (accessed 15 August 2016).
- Zhang M, Zupanski M, Kim M-J, Knaff JA. 2013a. Assimilating AMSU-A radiances in the TC core area with NOAA operational HWRF (2011) and a hybrid data assimilation system: *Danielle* (2010). *Mon. Weather Rev.* **141**: 3889–3907, doi: 10.1175/MWR-D-12-00340.1.
- Zhang SQ, Zupanski M, Hou AY, Lin X, Cheung SH. 2013b. Assimilation of precipitation-affected radiances in a cloud-resolving WRF ensemble data assimilation system. *Mon. Weather Rev.* **141**: 754–772, doi: 10.1175/MWR-D-12-00055.1.
- Zupanski D. 1993. The effects of discontinuities in the Betts–Miller cumulus convection scheme on four-dimensional variational data assimilation. *Tellus A* **45**: 511–524, doi: 10.3402/tellusa.v45i5.15053.
- Zupanski D, Zhang SQ, Zupanski M, Hou AY, Cheung SH. 2011. A prototype WRF-based ensemble data assimilation system for dynamically downscaling satellite precipitation observations. *J. Hydrometeorol.* **12**: 118–134, doi: 10.1175/2010JHM1271.1.